https://doi.org/10.5194/egusphere-2026-7007
Preprint. Discussion started: 24 November 2026
© Author(s) 2026. CC BY 4.0 License.

Targeted observations could substantially reduce aerosol radiative forcing uncertainty over China

Jianxing Luo[1], Leighton A. Regayre[2,3,4], Léa MC Prévost[3], Kunal Ghosh[3]

[1]Independent Researcher, China
[2]Met Office Hadley Centre, Exeter, Fitzroy Road, Exeter, Devon, EX1 3PB, UK
[3]School of Earth and Environment, University of Leeds, Leeds, LS2 9JT, UK
[4]Centre for Environmental Modelling and Computation, School of Earth and Environment, University of Leeds, Leeds, LS2 9JT, UK

Correspondence to: Leighton A. Regayre (L.A.Regayre@leeds.ac.uk)

Abstract. Aerosol radiative forcing remains one of the key uncertainties in climate models, limiting the accuracy of projections and weakening global action to mitigate climate risks. Previous studies combining observations with a perturbed parameter ensemble of the UK Earth System Model (UKESM1) identified and constrained the key causes of uncertainty, reducing global-mean aerosol forcing uncertainty by nearly 70 %. However, some regions remain highly uncertain after constraint, particularly over densely populated and industrialized East Asia. Here, we aim to further constrain the remaining uncertainty caused by aerosol-cloud forcing, quantify the constraint potential of novel observations, and guide future measurement strategies. We map regions over mainland China that remain highly uncertain after observational constraint, identify observation combinations that share causes of uncertainty with ΔF_{aci} and provide complementary information for constraint, then test their constraint potential using synthetic constraints. These synthetic constraints further reduce the remaining uncertainty by around 30 % over eastern coastal China and by around 50 % over central China. Our results also identify a lack of useful observations over the Tibetan Plateau in western China, providing clear priorities for future observational constraint. These results show that constraining aerosol forcing depends less on the number or spatial coverage of observations and more on making complementary collocated measurements at times and locations that directly target the key causes of model uncertainty. Our framework links diagnosis of remaining model uncertainty with observational strategy and subsequent constraint, providing actionable guidance for future aerosol observations and iterative model evaluation.

1 Introduction

Aerosol effective radiative forcing (ΔF_{aer}) is one of the largest and most persistent causes of uncertainty in anthropogenic climate change (Forster et al., 2021). Despite continued improvements in climate models and the increasing availability of observations, the uncertainty in historical ΔF_{aer} has persisted for several decades with little change (Gettelman et al., 2024; Carslaw et al., 2018). Anthropogenic aerosols offset some of the historical warming caused by greenhouse gases, so ΔF_{aer} uncertainty weakens confidence in near-term climate projections (Andreae et al., 2005; Seinfeld et al., 2016; Peace et al.,

https://doi.org/10.5194/egusphere-2026-7007
Preprint. Discussion started: 24 November 2026
© Author(s) 2026. CC BY 4.0 License.

2020; Fyfe et al., 2021). Constraining ΔF_{aer} uncertainty is essential to improve the accuracy of actionable information provided to governments, policymakers, and the public (Peace et al., 2020; Watson-Parris and Smith, 2022).

Aerosol effective radiative forcing can be separated into components caused by aerosol–cloud interactions (ΔF_{aci}) and aerosol–radiation interactions (ΔF_{ari}) (Forster et al., 2021). ΔF_{aci} is the larger and more uncertain component, accounting for 80% of the uncertainty in ΔF_{aer} (Regayre et al., 2023). Model uncertainty arises from parametrisations of aerosol, cloud, and atmospheric processes in global climate models, which control processes such as aerosol emissions and removal, particle size and composition, cloud droplet activation, and cloud microphysics. Increasing resolution is not a viable solution to these inherent uncertainties due to vast differences in scale between microphysical processes and model resolution (McCoy et al., 2025). Variations in these parameters can generate significant differences in simulated ΔF_{aer}(Carslaw et al., 2013; Regayre et al., 2018).

Observational constraints are affected by measurement uncertainty, as well as spatial and temporal representation errors (Schutgens et al., 2017). Model equifinality (Beven and Freer, 2001) also limits how effectively observations constrain model uncertainty (Lee et al., 2016), as do model structural deficiencies (Regayre et al., 2023; Prévost et al., 2026a). Observational campaigns may focus on specific aerosol processes or environments, but the measurements collected are not necessarily the most useful for reducing aerosol forcing uncertainty, and increasing the number and type of observations used for constraint does not automatically produce stronger forcing constraints as might be expected (Johnson et al., 2020; Prévost et al., 2026b). Thus, challenging models using available observations has not successfully reduced ΔF_{aci} uncertainty. New approaches are needed to identify observations with the greatest potential to constrain ΔF_{aci}.

Perturbed parameter ensembles (PPEs), combined with statistical emulators can be used to systematically explore the combined effects of dozens of uncertain model parameters across millions of model variants, to identify the parameters and processes responsible for ΔF_{aci} uncertainty (Carslaw et al., 2013; Carslaw et al., 2026; Bhatti et al., 2026; Regayre et al., 2014, 2015, 2023; Watson-Paris et al., 2020, Eidhammer et al., 2024, Yoshioka et al., 2019). Regayre et al. (2023; hereafter R23) evaluated over 450 observable variables over regions of persistent stratocumulus cloud. They only needed 13 observations in combination to 'optimally' constrain ΔF_{aci}, reducing global annual-mean ΔF_{aci} uncertainty by nearly 70 %. Regayre et al. (2026; hereafter R26) subsequently examined spatial diversity in the causes of the remaining ΔF_{aci} uncertainty. In some regions, most of the original uncertainty was removed, whereas a large fraction remained elsewhere, notably over highly populated and industrialized East Asia. This raises two practical questions: First, why was East Asian ΔF_{aci} uncertainty effectively unconstrained by the R23 'optimal' constraint? Secondly, which observations will most effectively constrain ΔF_{aci} over East Asia and thus the global mean ΔF_{aci}?

https://doi.org/10.5194/egusphere-2026-7007
Preprint. Discussion started: 24 November 2026
© Author(s) 2026. CC BY 4.0 License.

Here, we focus on three distinct regions within China, with high remaining uncertainty after the R23 'optimal' constraint. In Section 3.1, we quantify remaining ΔF_{aci} uncertainty over China after the optimal constraint. In Section 3.2, we identify three regions with distinct causes of ΔF_{aci} uncertainty and contrast these with the broader R26 focus areas. In Section 3.3 and Section 3.4, we identify target observations (specific types, locations, and timing) for additional ΔF_{aci} constraint, which we deploy in Section 3.5, using synthetic constraints to quantify constraint potential. In Section 3.6, we systematically evaluate the remaining ΔF_{aci} uncertainty after combining our targeted synthetic constraints with the R23 'optimal' constraint, noting changes in magnitude, spatial and seasonal distribution, and causes of remaining uncertainty. We make recommendations for novel observations at new and existing observation stations in Section 4.

2 Method

We used the PPE and statistical emulation methodology defined in R23. They perturbed 37 parameters related to aerosol, clouds, and radiation (see Sect. 2.1 and Appendix A). R26 identified key regions of shared causes of remaining annual mean ΔF_{aci} uncertainty after applying the R23 optimal constraint. We go further here by analysing shared causes of monthly mean ΔF_{aci} uncertainty across multiple observable variables.

We summarise the R23 experimental design in Section 2.1 and their approach to observational constraint in Section 2.2. In Section 2.3, we outline the spatial clustering method used to identify regions over China that share key causes of uncertainty. In Section 2.4, we outline our variance-based sensitivity analysis methodology, and in Section 2.5, our approach to selecting target months used for synthetic constraints. In Section 2.6, we detail how these priority constraint locations relate to existing meteorological stations. Finally, our methodology for applying synthetic constraints at the model grid box level is described in Section 2.7.

2.1 Experimental design

2.1.1 Model version

The PPE analysed here was created using version 1 of the UK Earth System Model (UKESM1; Sellar et al., 2019), which is based on the HadGEM3-GC3.1 physical climate model (Williams et al., 2018) and integrates the United Kingdom Chemistry and Aerosol (UKCA) model (Archibald et al., 2020). The atmosphere-only configuration (UKESM1-A) is composed of the GA7.1 atmospheric model (Walters et al., 2019), combined with aerosol, cloud, and physical atmosphere scheme updates as implemented in Mulcahy et al. (2020). R23 used the UKESM1-A version at N96 horizontal resolution (1.875° × 1.25°, approximately 208 km × 139 km near the equator), with 85 vertical levels unevenly distributed between the surface and 85 km in altitude. The configuration matches the model version submitted to the 6th Coupled Model Intercomparison Project

https://doi.org/10.5194/egusphere-2026-7007
Preprint. Discussion started: 24 November 2026
© Author(s) 2026. CC BY 4.0 License.

(CMIP6; Eyring et al., 2016). Horizontal wind fields above around 2 km were nudged towards ERA-Interim reanalysis data from December 2016 to November 2017, while prescribing sea ice and sea surface temperatures for the same period.

Each member of the PPE was forced using anthropogenic SO_2 emissions for the years 2014 and 1850, as prescribed in CMIP6 simulations. The ΔF_{aer} was estimated as the difference in top-of-the-atmosphere radiative fluxes between the two anthropogenic emission periods, accounting for above-cloud aerosol radiative effects (Ghan et al., 2016) and multiple cloud adjustments (Forster et al., 2021; Grosvenor and Carslaw, 2020) when decomposing ΔF_{aer} into components for ΔF_{aci} and ΔF_{ari}. Copernicus Atmosphere Monitoring Service (CAMS) data were used to prescribe present-day carbonaceous aerosol from biomass burning sources. Ocean surface concentrations of dimethyl sulfide (DMS) and chlorophyll, as well as atmospheric concentrations of gas-phase species, including OH and O_3, were derived from the multi-year monthly averages (1979-2014) of fully coupled UKESM1 simulations. Additionally, R23 prescribed volcanic SO_2 emissions for continuously emitting and sporadically erupting volcanoes (Andres and Kasgnoc, 1998) and for explosive volcanic eruptions (Halmer et al., 2002).

R23 applied additional structural changes to address known model deficiencies and better sample the breadth of uncertainty in UKESM1-A. They added a revised threshold for ice mass fraction above which nucleation scavenging is deactivated to allow aerosol transport into the Arctic (Browse et al., 2012). To improve aerosol absorption, they also updated high-resolution lookup tables for aerosol optical properties (Bellouin et al., 2013), including mineral dust (Balkanski et al., 2007). Additionally, to better represent remote marine and early industrial aerosol concentrations accurately in the model, which is known to affect the magnitude of ΔF_{aer} (Carslaw et al., 2013), R23 also included an organically mediated aerosol nucleation parameterisation (Metzger et al., 2010).

2.1.2 Perturbed parameter ensemble and statistical emulation

The R23 PPE consists of 221 model simulations and spans 37 perturbed parameters related to aerosols, clouds, and the physical atmosphere (detailed in Table A1). Parameters were chosen to sample uncertainty in processes related to structural model developments (Mulcahy et al., 2018, 2020; Walters et al., 2019) and insights from analysis of previous PPEs (Carslaw et al., 2013; Regayre et al., 2015, 2018; Sexton et al., 2021; Yoshioka et al., 2019). Their perturbation ranges were determined by formal expert elicitation, which was based on the Sheffield Elicitation Framework (SHELF) approach (Gosling, 2018).

We follow the R23 approach and use Gaussian Process emulators (O'Hagan, 2006) to extend the 221-member PPE to 1 million model variants (parameter combinations). Emulators efficiently predict output for new parameter combinations compared to running climate models. In contrast to other machine-learning approaches, emulator uncertainty is quantifiable,

https://doi.org/10.5194/egusphere-2026-7007
Preprint. Discussion started: 24 November 2026
© Author(s) 2026. CC BY 4.0 License.

enabling rapid validation of emulator skill and avoidance of over-constraint when comparing model variant output to observations (e.g., Johnson et al., 2020).

2.2 Observational constraint

Regayre et al. (2023) constrained ΔF_{aci} using multiple satellite observational variables of cloud and radiation properties. Based on the original set of 1 million model variants of ΔF_{aci}, R23 explored the constraint potential of observations and, through pairwise consistency with cloud droplet number concentration (N_d), identified multiple variables associated with model structural deficiencies. Corresponding observations were removed from the R23 constraint. Of the remaining 225 observations, R23 identified the single observation that produced the greatest reduction in the 90% credible interval of ΔF_{aci}. Observational constraints were then progressively added to produce the tightest constraint. At each stage, at least 5000 model variants were retained to avoid over-constraint. Ultimately, the R23 optimal constraint was achieved using only 13 observation values, spanning multiple observation types, regions, and seasons. The final set of 5000 model variants was defined to be "optimal". We use the R23 optimal constraint sample of 5000 model variants as the basis for our subsequent analysis of remaining ΔF_{aci} uncertainty and potential for additional constraint over China.

2.3 Regional clusters of shared causes of uncertainty

R26 applied K-means clustering, an unsupervised machine learning technique, to group model grid boxes into regions of shared causes of annual mean ΔF_{aci} parametric uncertainty. The clustering was based on percentage contributions to variance multiplied by the sign of variable response to increasing parameter values from the high-dimensional non-linear fit to each variable (Sect. 2.4). Our analysis focuses on the target clusters over China with relatively high remaining uncertainty.

The global cluster map created by R26 partitioned the Asian region into three clusters. We retain the cluster subsets located over mainland China and refer to them hereafter as Cluster 1 (polluted; updraft-limited), Cluster 2 (polluted; mixed aerosol composition), and Cluster 3 (clean; dynamically sensitive and aerosol-limited). Cluster membership is taken directly from the annual mean R26 clusters, which maintains the link to causes of global uncertainty. To characterize parametric uncertainty within the redefined target clusters, rather than across the full spatial extent of the corresponding R26 global cluster, which includes geographically remote regions, we re-quantify the contributions of all 37 uncertain parameters to the remaining ΔF_{aci} variance (Section 2.4).

2.4 Causes of remaining uncertainty

Following R26 and Prévost et al. (2026), we use Generalised Additive Models (GAMs) to quantify the importance of the 37 parameters as causes of model uncertainty using variance-based sensitivity analyses. GAMs are well suited to capturing high-dimensional parameter responses within heterogeneously distributed data. In other words, we can still perform robust

https://doi.org/10.5194/egusphere-2026-7007
Preprint. Discussion started: 24 November 2026
© Author(s) 2026. CC BY 4.0 License.

sensitivity analyses after applying observational constraints that rule out parts of parameter space as observationally implausible. We fit non-linear GAMs to model output of ΔF_{aci} and observable model variables at the grid box level using the pygam Python package (Servén and Brummitt, 2018).

We quantify the variance in model output attributable to each parameter by varying one parameter value across its uncertain range while the remaining 36 parameters are held at their median values. Marginal variances from all 37 parameters are treated additively to define the total parametric variance. The relative contribution of each parameter is calculated as its marginal variance divided by the total variance and expressed as a percentage. This approach neglects parameter interaction effects but is suitable for sensitivity analyses over observationally constrained parameter spaces. These relative contributions to remaining variance reflect the local sensitivity of the model output to changes in each parameter.

The GAMs were trained on the 'optimal' set of 5000 model variants as defined in R23 (Section 2.2). Here, we applied the GAM sensitivity analysis approach to monthly and annual-mean ΔF_{aci}, together with monthly mean values of seven observable model variables related to aerosol-cloud-radiation processes: cloud droplet concentration (N_{d}), aerosol optical thickness (AOD) at 550 nm, absorbing aerosol optical thickness (AAOD) at 550 nm, and near-surface concentrations of sulfuric acid (H_2SO_4), sulfur dioxide (SO_2), black carbon (BC), and organic carbon (OC).

2.5 Target month selection

Regayre et al. (2023) showed there is substantial redundancy in the potential to constrain models using monthly mean observation data. To further our aim of constraining remaining annual mean ΔF_{aci} uncertainty, we first identify months with the greatest constraint potential within each cluster. Constraint potential is quantified using cluster-mean remaining uncertainty after R23 constraint, and overlap in causes of uncertainty with annual-mean ΔF_{aci} (our constraint target). Overlap between causes of uncertainty is quantified using Lin's concordance correlation coefficient (CCC; Lin, 1989) across the subset of parameters that contribute at least 2 % of the remaining annual-mean ΔF_{aci} uncertainty. We use Lin's CCC because it is designed to quantify how closely two sets of measurements agree, rather than simply how strongly they correlate. Its main advantage over, say Pearson's correlation coefficient is that it penalises systematic differences between datasets, including differences in their mean and variance (Pearson, 1896). Remaining ΔF_{aci} uncertainty within the optimally constrained set of variants is quantified as the cluster-mean 90% credible interval ranges, calculated from monthly mean data across all the grid boxes within a cluster. Equal weighting was given to normalised values of (a) overlap and (b) variance metrics when ranking months according to additional constraint potential. For each target cluster, the three months with the highest combined scores were selected as target months for additional constraint analysis.

https://doi.org/10.5194/egusphere-2026-7007
Preprint. Discussion started: 24 November 2026
© Author(s) 2026. CC BY 4.0 License.

2.6 Candidate observation locations

We evaluate the availability of in-situ observations and contrast them with idealised synthetic constraints in target locations. Our hypothesis is that existing stations will have lower constraint potential than idealised synthetic observations placed at locations where the causes of uncertainty are most similar to those of the whole region we aim to constrain, as quantified using the approach outlined in Section 2.5. However, collecting additional key observations at existing stations would be more cost-effective than installing new observation platforms that align perfectly with our synthetic constraints. Existing station information was compiled from the Sun–Sky Radiometer Observation Network (SONET) and the Campaign on Atmospheric Aerosol Research network of China (CARE-China) (Li et al., 2018; Xin et al., 2015). SONET provides long-term ground-based observations of aerosol optical, physical, and radiative properties at distributed sites across China, while CARE-China was established as a nationwide network for coordinated measurements of aerosol physical, chemical, and optical properties, as well as related atmospheric components. Stations appearing in both networks were treated as a single location. Each station was assigned to the overlapping model grid box to determine its membership in the target cluster and extract the corresponding model results.

We identified which four parameters contribute most to model uncertainty, for each of the target months within each cluster, by first calculating the cluster-mean contributions of each of the 37 parameters to the remaining ΔF_{aci} variance, after R23 constraint. We then quantified the degree of similarity between cluster-mean and individual grid box causes of uncertainty using the same CCC metric used to quantify similarity between monthly and annual mean ΔF_{aci} causes of uncertainty (Section 2.5). We classified grid boxes with CCC values greater than 0.9 as 'highly representative' of the cluster-wide causes of uncertainty – reducing uncertainty in these target grid boxes, in the identified months, will most likely reduce uncertainty across the cluster. Model grid boxes with high cluster-mean representativeness in at least one of the three target months could be placed idealised synthetic constraints. However, some representative grid boxes that lack coverage by existing stations are considered as potential new observation sites. In evaluating these sites, we additionally considered the geographical setting of each candidate area, including proximity to cities or towns for ease of station maintenance, and broader field feasibility, to ensure that any recommended locations are not only representative of the cluster-wide causes of uncertainty but also practically suitable for ground-based observations.

2.7 Synthetic constraints

We constructed synthetic observations to quantify the maximum feasible reduction in ΔF_{aci} that could be achieved using observations at target months and candidate locations (Section 2.5 & 2.6). We used the 5000 model variants from the R23 optimal constraint as a basis for applying additional synthetic constraints.

https://doi.org/10.5194/egusphere-2026-7007
Preprint. Discussion started: 24 November 2026
© Author(s) 2026. CC BY 4.0 License.

For each target cluster and month (Section 2.3 & 2.5), we used the value of a single model variant to represent the synthetic observation. This idealised approach using self-consistent model output is not limited by structural model deficiencies that may otherwise prevent observations from providing an effective constraint (Regayre et al., 2023; Prévost et al., 2026a). We selected the model variant, from the 5000 variants, with the smallest Euclidean distance from the centre of the normalised 37-dimensional parameter space, representing a model with parameter settings most similar to the R23 optimally constrained set of model variants. Alternative synthetic constraints, such as an extreme parameter combination, will almost certainly alter the magnitude of constraint. However, our interest here is to evaluate the potential for targeted observational constraints to significantly reduce persistent uncertainty, and for such a purpose a synthetic observation towards the centre of our output space is sufficient.

We quantified the agreement between values for each of the 5000 model variants and the synthetic observation using a normalised absolute distance metric. That is, the distance between each synthetic observation and model variants was normalised by the 90 % credible interval range across the 5000 variants. For combinations of synthetic observations within a target cluster and month, we calculated the mean normalised absolute distance across selected observables (Section 2.4) and used this to rank model variants from most- to least-similar to the synthetic constraint. Some compensation is expected when variables are combined because our synthetic constraints are independent (Regayre et al., 2023), so they are not overall self-consistent as a constraint.

For each target cluster, synthetic constraints were applied using combinations of observable variables. Variable combinations were applied independently to the full set of 5000 model variants, with synthetic observations added progressively. For each variable added to the combination of constraints, we retained the closest 4000 model variants to evaluate the constraint performance of each combination and identify the most effective variable set. To quantify the contribution of each additional synthetic observable, we compared the reduction in the 90 % credible interval range of the cluster mean ΔF_{aci} uncertainty for each additional variable with the preceding combination at the same retained ensemble size. We first identified and applied the synthetic observation that achieved the strongest constraint on remaining ΔF_{aci} uncertainty, then progressively added constraints until no remaining observable further reduced the cluster-mean 90 % credible interval range. The 1000 closest model variants for this combination were then retained as the final tight synthetic constraint ensemble, which assumes observational uncertainties, representation errors, and other practical sources of mismatch have been addressed, and used for consistent subsequent analysis across clusters.

3 Results

We frame our evaluation of the processes that further constrain the remaining ΔF_{aci} uncertainty over China, complementing the R23 optimal constraint, in three stages:

https://doi.org/10.5194/egusphere-2026-7007
Preprint. Discussion started: 24 November 2026
© Author(s) 2026. CC BY 4.0 License.

1. Quantify the remaining ΔF_{aci} uncertainty (Section 3.1) and identify key causes of uncertainty within the three target clusters over mainland China (Section 3.2).

2. Identify target months and candidate observation locations to maximise synthetic observational constraint of ΔF_{aci} (Section 3.3 and 3.4).

3. Apply the synthetic constraint within the target clusters (Sect. 3.5). We further explore the effects of the synthetic constraints in Section 3.6.

3.1 Remaining ΔF_{aci} uncertainty over China after optimal constraint

Aerosol forcing is strongly influenced by anthropogenic emissions over mainland China, where the R23 optimal constraint only reduced regional mean ΔF_{aci} uncertainty by around 30 % or less (R26). Figure 1a shows the magnitude of annual mean ΔF_{aci} uncertainty over China in the original unconstrained set of 1 million model variants at grid-box level. The greatest ΔF_{aci} uncertainty is located around the Sichuan Basin, where peak uncertainty reaches 30 W m^{-2}. The central, eastern, and coastal regions of China also have relatively high uncertainty, with ΔF_{aci} values ranging from 5 to 20 W m^{-2}. Although the uncertainty in the northwest and northeast regions of China is lower than in other areas, it is still relatively high compared to other regions (Regayre et al., 2026) and generally greater than 5 W m^{-2}. In contrast, the remaining uncertainty in the western plateau region is relatively low, with credible interval ranges around 4 W m^{-2} or less. This western plateau region is less affected by the R23 optimal constraint (Fig. 1c), but the unconstrained ΔF_{aci} uncertainty in this area was lower than 5 W m^{-2}.

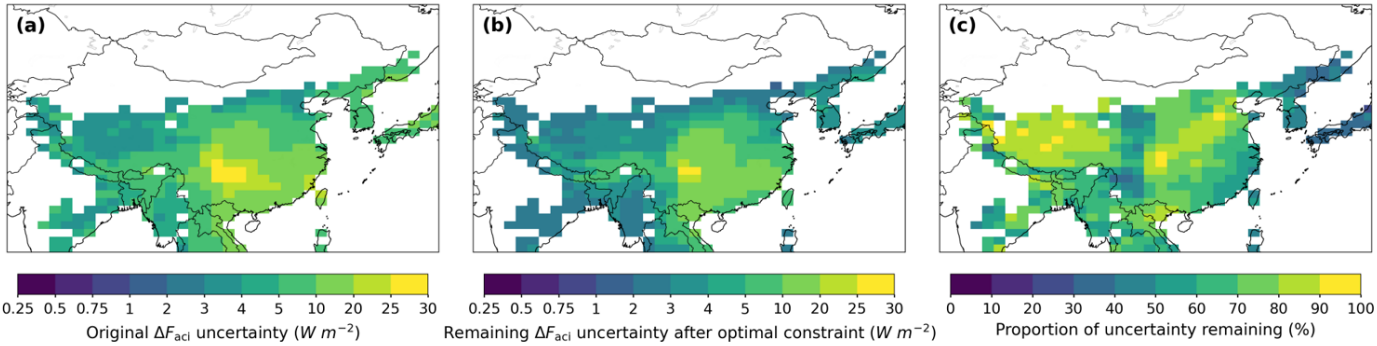


Figure 1:Annual mean ΔF_{aci} uncertainty (90 % credible interval ranges) in model grid boxes within mainland China from (a) the original set of 1 million model variants, and (b) the R23 optimally constrained set of model variants, and (c) the proportion of original uncertainty remaining after optimal constraint. The masked area represents the grid points where the remaining uncertainty of ΔF_{aci} is lower than 0.5 W m^{-2}.

https://doi.org/10.5194/egusphere-2026-7007
Preprint. Discussion started: 24 November 2026
© Author(s) 2026. CC BY 4.0 License.

Remaining ΔF_{aci} uncertainty over China after the R23 optimal constraint, and the ratio of remaining to original uncertainty, are shown in Fig. 1b and Fig. 1c. The optimal constraint has the greatest effect near coastal areas and in parts of western and northwestern China. In these subregions, around 40 % of the original uncertainty is constrained. In contrast, the constraints imposed on ΔF_{aci} in other regions in China are significantly weaker. Figure 1c shows a distinct band extending eastward from the Sichuan Basin across central China, where more than 80% of the original uncertainty remains. These results highlight the potential to further constrain the remaining ΔF_{aci} uncertainty over China using additional, targeted observations.

3.2 Causes of remaining ΔF_{aci} uncertainty within target clusters

Regayre et al. (2026) demonstrated that the relative importance of uncertain parameters varies significantly between regions, and some parameters that have already been effectively constrained on a global scale may still be significant causes of uncertainty at the regional scale. Figure 2 shows the spatial distribution of the three target clusters and the average parameter contributions to remaining ΔF_{aci} uncertainty in each cluster. The key uncertain parameters in Clusters 1 and 2 remain unchanged from similar clusters that spanned multiple geographical regions in R26 (see Figs. A1 & A2). However, the relative contributions of these parameters are distinct in our China-focused clusters, because the average causes of uncertainty are not influenced by comparable parameter-driven ΔF_{aci} responses in other parts of the world. In contrast, the key uncertain parameters in Cluster 3 differ from those in the corresponding R26 cluster, suggesting this region represents distinct causes of remaining ΔF_{aci} uncertainty that are not resolved at the current level of clustering (see Figs. A3). That is, of the three clusters evaluated here, constraint within Cluster 3 is least likely to feed through to global mean constraint. Clusters defined within the boundaries of mainland China therefore provide the clearest opportunity to evaluate the potential for additional ΔF_{aci} constraint in this region. In the three target clusters over China, the four largest contributing parameters in each cluster cause more than half of the remaining ΔF_{aci} uncertainty (around 58 %, 70 %, and 56 % in Clusters 1, 2, and 3, respectively). Therefore, we use the four most sensitive parameters to characterize parametric causes of uncertainty for each cluster.

https://doi.org/10.5194/egusphere-2026-7007
Preprint. Discussion started: 24 November 2026
© Author(s) 2026. CC BY 4.0 License.

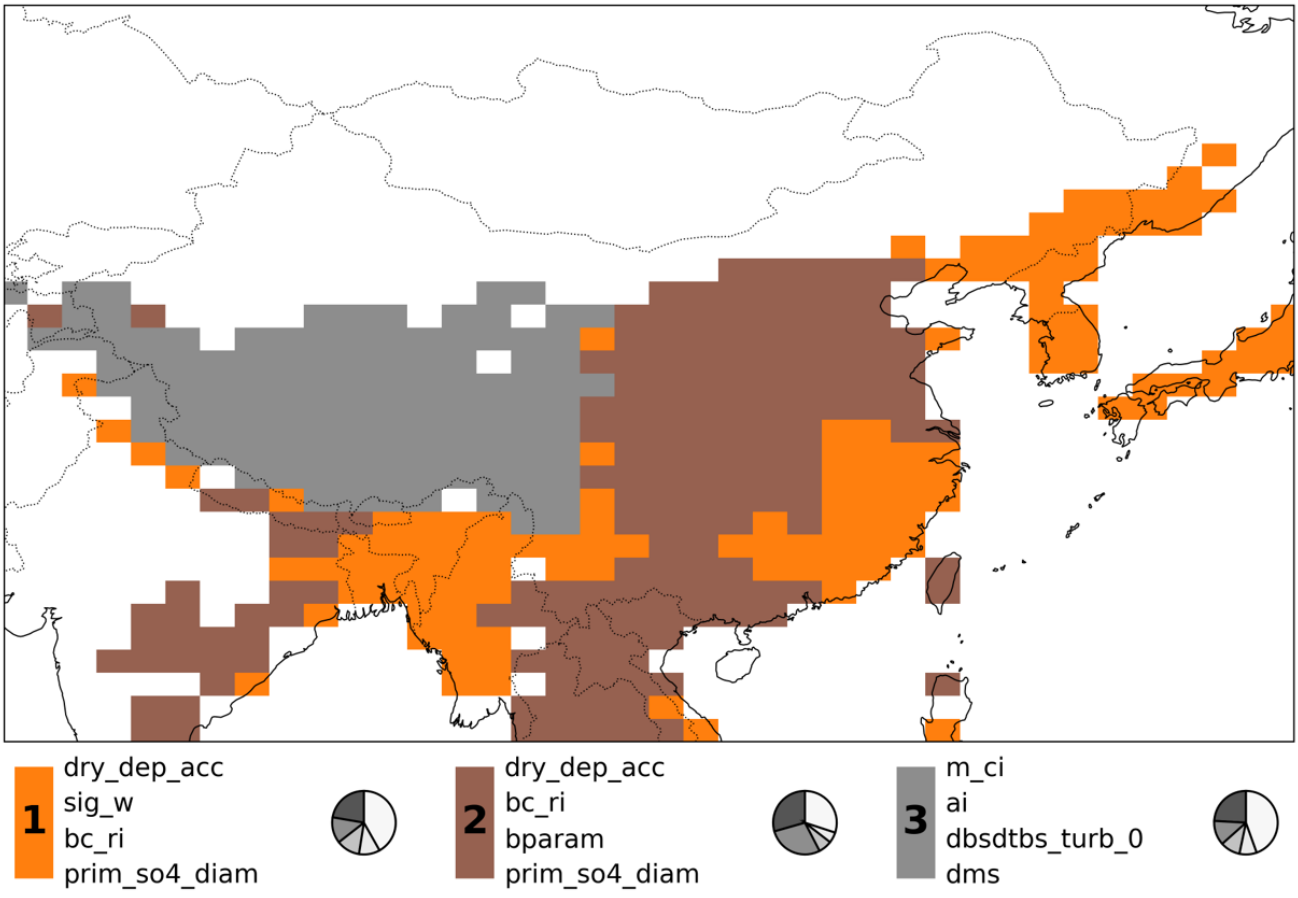


Figure 2: Clusters of shared causes of remaining ΔF_{aci} uncertainty over mainland Central Asia, after the R23 optimal constraint. Grid points where the remaining uncertainty of ΔF_{aci} is lower than 0.5 W m^{-2} are masked. Legends for each cluster show the four most important parameters in each cluster according to their relative contributions to the remaining ΔF_{aci} uncertainty. Pie charts show the proportion of variance caused by each parameter in a counterclockwise direction, with the white area representing the combined contribution of the remaining 33 parameters.

Cluster 1 (polluted; updraft-limited) covers much of eastern and northeastern China, with additional regions in the southwest. Remaining ΔF_{aci} uncertainty is dominated by aerosol deposition (*dry_dep_acc;* 22 %), cloud droplet activation (*sig_w;* 13 %), radiative properties of BC aerosol (*bc_ri;* 12 %), and dry diameter of newly formed sulfate aerosol (*prim_so4_diam;* 11 %). Increasing aerosol removal rates reduces baseline aerosol concentrations and makes clouds more susceptible to aerosol changes caused by increasing anthropogenic pollution sources, thereby strengthening ΔF_{aci} over the historical period (Carslaw et al., 2013). However, the sign of this effect may change with the seasons due to source variations (Regayre et al., 2015). At relatively high aerosol concentrations, droplet activation becomes increasingly limited by updraft velocity. Thus, the importance of the *sig_w* parameter, which affects the number of particles activated into cloud droplets and impacts the simulation of N_d, suggests Cluster 1 has relatively high aerosol concentrations.

https://doi.org/10.5194/egusphere-2026-7007
Preprint. Discussion started: 24 November 2026
© Author(s) 2026. CC BY 4.0 License.

BC absorption (*bc_ri* parameter) alters the vertical heating profile of the atmosphere potentially affecting convection, boundary layer stability, cloud cover, and other cloud radiation properties (Regayre et al., 2018), including cloud depth (Bond et al., 2013; Zhuang et al., 2010). The emission diameter of newly formed sulfate particles is strongest in polluted regions (R26). We are aware that China's clean air actions substantially reduced anthropogenic aerosol and precursor emissions, with declines in SO_2, BC, OC, and $PM_{2.5}$ over eastern China from 2013 to 2019 (Gao et al., 2023). Although reductions in anthropogenic aerosol emissions have altered the aerosol background in this region, we expect the same key parameters to remain important even if the analysis period were changed. Collectively, the importance of these 4 key parameters as causes of remaining ΔF_{aci} uncertainty in Cluster 1 indicates ΔF_{aci} is sensitive to anthropogenic aerosol properties and processing in this relatively polluted region. Henceforth, we refer to this cluster as a polluted, updraft-limited region. As such, we hypothesise there is excellent potential for further constraint.

Cluster 2 (polluted; mixed aerosol composition) covers most of central China and contains the region of highest remaining ΔF_{aci} uncertainty after optimal constraint (Fig. 1b). The *dry_dep_acc* and *bc_ri* parameters cause around 29 % and 28 % of the remaining uncertainty respectively (58 % when combined). As in Cluster 1, the importance of these two parameters suggests that ΔF_{aci} in Cluster 2 is a polluted region. The carbonaceous aerosol parameter, *bc_ri,* causes far more ΔF_{aci} uncertainty in Cluster 2, indicating that uncertainty in the model representation of black-carbon radiative properties is especially important in central China. Smaller contributions to remaining uncertainty are made by the remaining two top parameters in Cluster 2; around 7 % from the *bparam* parameter and 5 % from the *prim_so4_diam* parameter. The *bparam* parameter is used in the model calculation of cloud effective radius, which contributes to ΔF_{aci} uncertainty by altering the cloud properties and hence the modelled susceptibility of clouds to aerosol perturbations. Lower values of *prim_so4_diam* (the diameter of primary sulfate particles) increase aerosol concentrations, leading to stronger competition for available moisture and smaller cloud droplets that are less likely to form raindrops. Based on this, we refer to this cluster as a polluted, mixed aerosol composition region. Similar to Cluster 1, the four parameters identified as key causes of uncertainty in Cluster 2 suggest the remaining uncertainty in this region may be further constrained using existing or novel local observations.

Cluster 3 (clean; dynamically sensitive and aerosol-limited) is located over western and northwestern China. Remaining ΔF_{aci} uncertainty is sensitive to a distinct combination of parameters than other clusters. The most important parameter scales the modelled ice fall speed (*m_ci;* 24 %), whilst other parameters affect ice-particle mass (*ai;* 13 %), cloud erosion rates (*dbsdtbs_turb_0;* 10 %) and emissions of dimethylsulfide (*dms;* 9 %). These causes of remaining ΔF_{aci} uncertainty suggest Cluster 3 uncertainty is controlled by the model representation of cloud and microphysical processes. Hence, we refer to Cluster 3 as a clean, dynamically sensitive and aerosol-limited region. Cluster 3 may therefore not be as receptive to additional constraints using near-surface aerosol concentrations, nor vertical column observations like AOD, but may respond to N_{d} observations, since Nd depends on both aerosol size, composition, and atmospheric conditions.

https://doi.org/10.5194/egusphere-2026-7007
Preprint. Discussion started: 24 November 2026
© Author(s) 2026. CC BY 4.0 License.

3.3 Identifying target months

Our aim is to identify target months when additional observations could most effectively constrain annual mean ΔF_{aci} uncertainty in each cluster. The causes of ΔF_{aci} uncertainty vary temporally due to changes in atmospheric conditions, aerosol emissions, and dominant processes (Regayre et al., 2015). That is, the choice of observation months is important because even within clusters that share key causes of annual mean uncertainty, model sensitivity to these parameters can vary seasonally across the year. Additionally, model responses to changes in multiple parameters may differ, even where the model is sensitive to the same parameters in the same proportions. So, constraining using a single month may not sufficiently constrain complex parameter dependencies. Choosing an observation month at random in a year from within a cluster will not automatically reduce uncertainty maximally across all the time. In addition, year-round observations may incur substantially higher costs and can be limited by practical constraints on continuous measurements. Thus, we identify only three observation months that best represent cluster-wide sensitivity to key parameters across the year in this section.

https://doi.org/10.5194/egusphere-2026-7007
Preprint. Discussion started: 24 November 2026
© Author(s) 2026. CC BY 4.0 License.

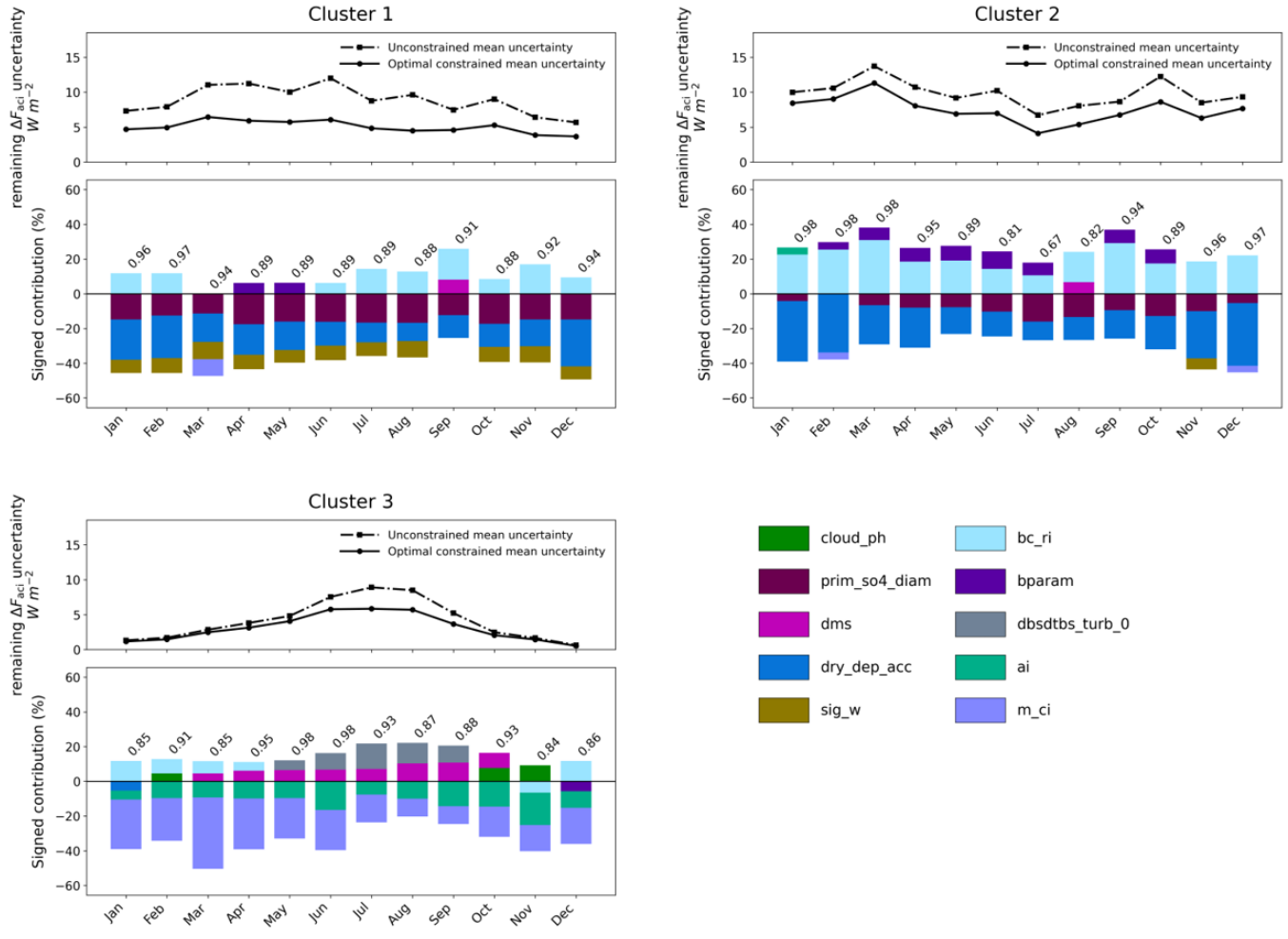


Figure 3: Seasonal variation in the remaining ΔF_{aci} uncertainty and percentage contributions to uncertainty across the three mainland China clusters. The top panels show the cluster mean ΔF_{aci} uncertainty of each cluster. The lower panels show the monthly parameter contributions after the optimal constraint. Only four parameters with the largest absolute contributions to ΔF_{aci} variance are shown for each month. Positive and negative contributions are stacked separately, with the sign determined from the response to increasing parameter values. Above each bar, we show the CCC value, which quantifies the agreement between the monthly parameter-contribution structure of the corresponding month and the annual mean.

Figure 3 shows the seasonal variation in the remaining ΔF_{aci} uncertainty after the R23 optimal constraint and the key causes of the remaining uncertainty across the three target clusters. There is a high degree of consistency in the causes of ΔF_{aci} uncertainty within each cluster. That is, the same key parameters cause ΔF_{aci} uncertainty in most months. The CCC values shown in Fig. 3 indicate the degree of similarity between the monthly and annual-mean uncertainty parameter contribution structures (See Fig. A4 for annual-mean sensitivities). Overall, the monthly results show that the main processes causing the annual mean remaining uncertainty remain important through much of the year. However, their relative

https://doi.org/10.5194/egusphere-2026-7007
Preprint. Discussion started: 24 November 2026
© Author(s) 2026. CC BY 4.0 License.

uncertainty contributions vary seasonally with CCC values ranging from 0.67 to 0.98, as a result of additional parameters becoming important in isolated months.

Figures 3 and A4 show that the annual-mean remaining ΔF_{aci} uncertainty contribution of an individual parameter is not simply the average of its 12 contributions to monthly mean uncertainty. Some parameters contribute a much larger proportion of the remaining ΔF_{aci} uncertainty in individual months than in the annual mean results (e.g. the black carbon absorption parameter, *bc_ri* in Clusters 1 and 3), whilst other parameters contribute consistently across months (e.g. the updraft velocity parameter, *sig_w* in Cluster 1). Thus, to provide additional information at the monthly mean scale for constraining remaining annual-mean ΔF_{aci} uncertainty, we need to identify combinations of months that each have high remaining uncertainty while also sharing parameter sensitivities with the annual mean (Section 2.5).

The remaining ΔF_{aci} uncertainty in Cluster 1 is affected by *dry_dep_acc*, *sig_w*, and *prim_so4_diam* parameters in all months, with similar sensitivities as the annual mean ΔF_{aci}. The *bc_ri* parameter shows a high degree of seasonal variation, contributing most to Cluster 1 ΔF_{aci} uncertainty in months when local burning rates are highest. However, the contribution of remaining uncertainty due to *bc_ri* does not simply follow seasonal changes in black carbon (BC) concentration. Enhanced burning and transport across the wider Asian region during March to April can increase BC concentrations without increasing the contribution to ΔF_{aci} uncertainty of the absorption parameter. That is, the relative importance of this parameter is suppressed when carbonaceous concentrations are very high. Other causes of uncertainty are important in particular months, indicating these months are a lower priority for further constraint due to a lack of representativeness of the annual mean ΔF_{aci} within the cluster. CCC values remain high from January to March and from November to December, with February showing the strongest agreement with the annual-mean result (CCC = 0.97). CCC values are slightly lower from April to October when other causes of uncertainty emerge, but these months still show strong similarity with the annual mean (CCC values of 0.88 and larger). After the optimal constraint, the cluster-mean ΔF_{aci} uncertainty in Cluster 1 reaches its highest value in March (6.45 W m^{-2}) and remains relatively high from April to June. Taken together, we identify March, June, and April as the priority target months for Cluster 1, which have greater potential for further observational constraint.

In Cluster 2, the *dry_dep_acc* and *bc_ri* parameters affect the remaining ΔF_{aci} uncertainty in most months, which is consistent with the annual mean sensitivities. However, both parameters show a clear seasonal pattern with higher contributions in winter when weaker wet scavenging and boundary-layer mixing favour higher aerosol concentrations and sizes near the surface. The correlation between monthly and annual mean sensitivities is highest from January to March, with CCC values of 0.98. Some of these months have unique additional parameter contributions to remaining ΔF_{aci} uncertainty, yet the sensitivities of key causes of uncertainty are aligned with the annual mean sensitivities. In contrast, monthly mean alignment with annual mean sensitivities is substantially lower during summer, reaching the lowest value in July (CCC = 0.67). The same four key causes of remaining annual mean ΔF_{aci} uncertainty also cause uncertainty in July, though the

https://doi.org/10.5194/egusphere-2026-7007
Preprint. Discussion started: 24 November 2026
© Author(s) 2026. CC BY 4.0 License.

relative importance of parameters shifts. In the annual mean, the aerosol removal parameter, *dry_dep_acc*, and the primary sulfate diameter parameter, *prim_so4_diam*, contribute around 29 % and 5 % of the uncertainty respectively. Whereas, in July they cause around 10 % and 20 % respectively. Thus, July observations may still provide useful constraints on the annual mean ΔF_{aci}. However, after the optimal constraint, the cluster-mean remaining ΔF_{aci} uncertainty in Cluster 2 is lowest in July and neighbouring summer months. Remaining uncertainty is highest in March (11.32 W m^{-2}) and remains relatively high in January and February. Hence, by jointly considering shared sensitivities and magnitude of remaining uncertainty, we select March, February, and January as the priority target months for Cluster 2.

Cluster 3 has the strongest seasonal variation in both the magnitude of remaining ΔF_{aci} uncertainty and causes of uncertainty. Remaining uncertainty is lower than a few W m^{-2} in winter months, so we restrict our target month selection to other months. Correlations between monthly and annual mean parameter sensitivities are highest from April to October, peaking in June (CCC = 0.98). Remaining cluster-mean ΔF_{aci} uncertainty peaks in July (5.85 W m^{-2}), and is higher than 5 W m^{-2} from June to August. Based on these results, we select June, July, and August as target months, which we consider to have the greatest potential for further observational constraint in Cluster 3. In these months, observations have potential to constrain parameters related to ice processes (*m_ci* and *ai*), cloud erosion (*dbsdtbd_turb_0*), and dimethyl sulfide emissions (*dms*), which are the four key causes of remaining annual mean uncertainty in Cluster 3.

3.4 Identifying candidate observation locations

In this section, we identify target locations where additional observations could most effectively constrain ΔF_{aci} uncertainty in each cluster for target months. Due to changes in atmospheric conditions, and aerosol emission sources, the causes of ΔF_{aci} uncertainty vary spatially within clusters. The choice of observation location is important because even within clusters that share key causes of uncertainty, model sensitivity to these parameters can vary with local conditions. That is, the same key parameters will affect ΔF_{aci} across a cluster, but exact percentage contributions will likely differ between neighbouring grid boxes. Choosing an observation location at random from within a cluster, or choosing a location towards the geographical centre of the cluster, will not automatically reduce uncertainty maximally across the entire cluster. Thus, our aim here is to identify observation locations that represent cluster-wide sensitivity to key parameters.

https://doi.org/10.5194/egusphere-2026-7007
Preprint. Discussion started: 24 November 2026
© Author(s) 2026. CC BY 4.0 License.

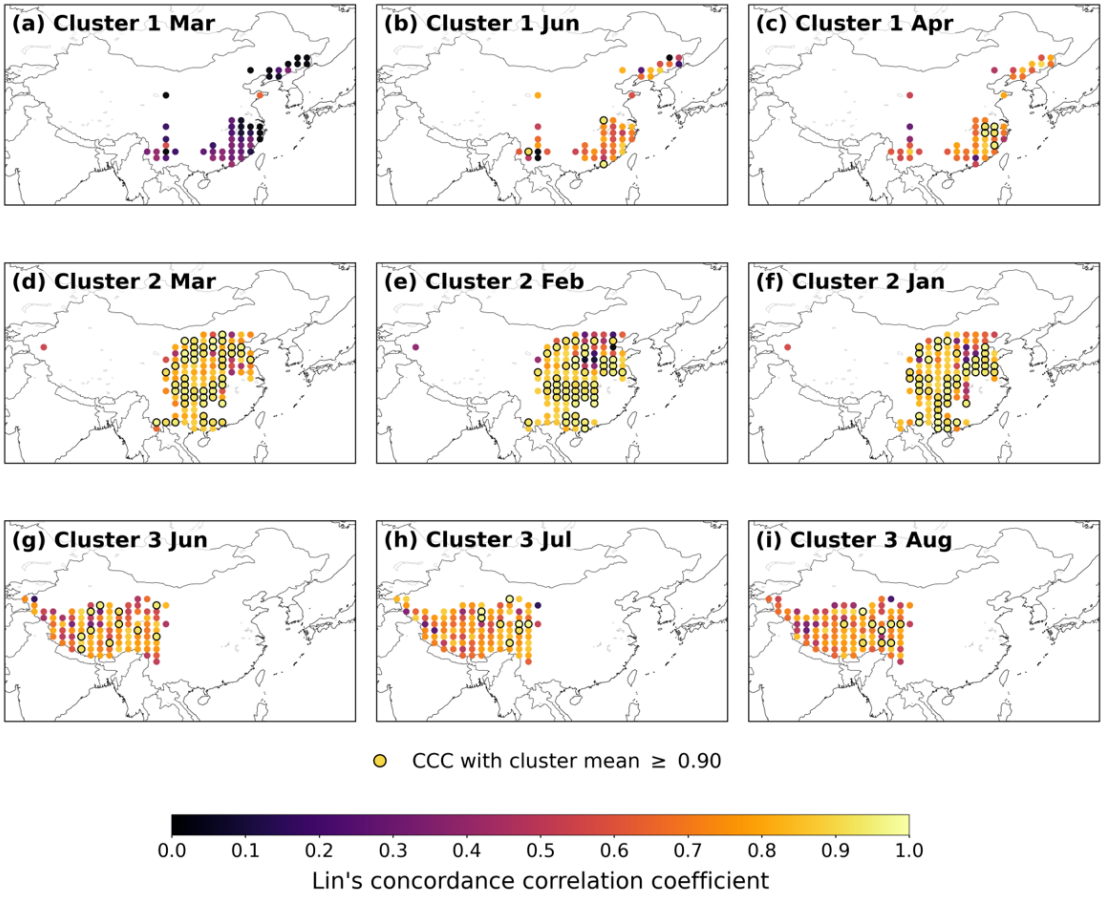


Figure 4: Model grid box representativeness of cluster-wide causes of ΔF_{aci} uncertainty for selected target months in each cluster. Shading shows CCC values. Circles are placed over grid boxes with CCC ≥ 0.9.

435

Figure 4 shows strong seasonal and spatial variation in target locations within each cluster. In Cluster 1, grid boxes with high cluster-mean representativeness (CCC ≥ 0.90) are relatively sparse. A few isolated locations are identified as highly representative in June and April, yet none are identified in March, where grid box CCC values are all less than 0.9 and typically less than 0.4. This suggests Cluster 1 may benefit from being dissected into sub-regions of distinct parameter
440 sensitivities for March. However, we will base our analysis on suitable locations identified in June and April. In contrast, Cluster 2 has a spatially coherent group of highly representative grid boxes in all three target months, particularly across central and southern China, including locations within the band of relatively high remaining uncertainty identified in Section 3.1 (Fig. 1c). Locations in Cluster 3 with relatively high representativeness of cluster-mean sensitivities are mainly concentrated in the Qinghai-Xizang Plateau and its surrounding areas. These results confirm our hypotheses that the final set
445 of existing and recommended sites that can best represent the entire cluster's constraint potential are not necessarily located close to the geographical center of the cluster, and the optimal location for observations will change seasonally.

https://doi.org/10.5194/egusphere-2026-7007
Preprint. Discussion started: 24 November 2026
© Author(s) 2026. CC BY 4.0 License.

Previous aerosol network studies have similarly used spatial representativeness to identify locations where observations provide more information about the broader aerosol environment (Moosavi et al., 2015). The spatial representativeness of observations is important when relating individual ground-based sites to regional or model-grid-scale behaviour, because measurements at a single location do not necessarily represent the surrounding larger spatial domain (Schutgens, 2020). We therefore further refine our evaluation of representative grid boxes to account for locations of existing aerosol observation sites. This allows us to identify (a) where existing observation data could be used for additional ΔF_{aci} constraint, and (b) locations where novel observations could maximise ΔF_{aci} constraint.

Existing SONET and CARE-China stations are prioritized as candidate sites for observational constraint if located in highly representative areas during at least one of the three selected target months. Existing sites overlap substantially with representative locations in Cluster 2, whereas Clusters 1 and 3 have no overlap due to the sparsity of both highly representative locations and existing stations in these clusters (Fig. 5 and Table A2). We therefore make recommendations for new observation station locations based on grid box representativeness of cluster-mean sensitivities during target months. Figure 5 shows the existing and novel observation locations identified for each target cluster using the approach described above. We hypotheses observations in these locations will provide an equitable and cost-effective ΔF_{aci} constraint compared to maximizing the number or geographical spread of observations.

https://doi.org/10.5194/egusphere-2026-7007
Preprint. Discussion started: 24 November 2026
© Author(s) 2026. CC BY 4.0 License.

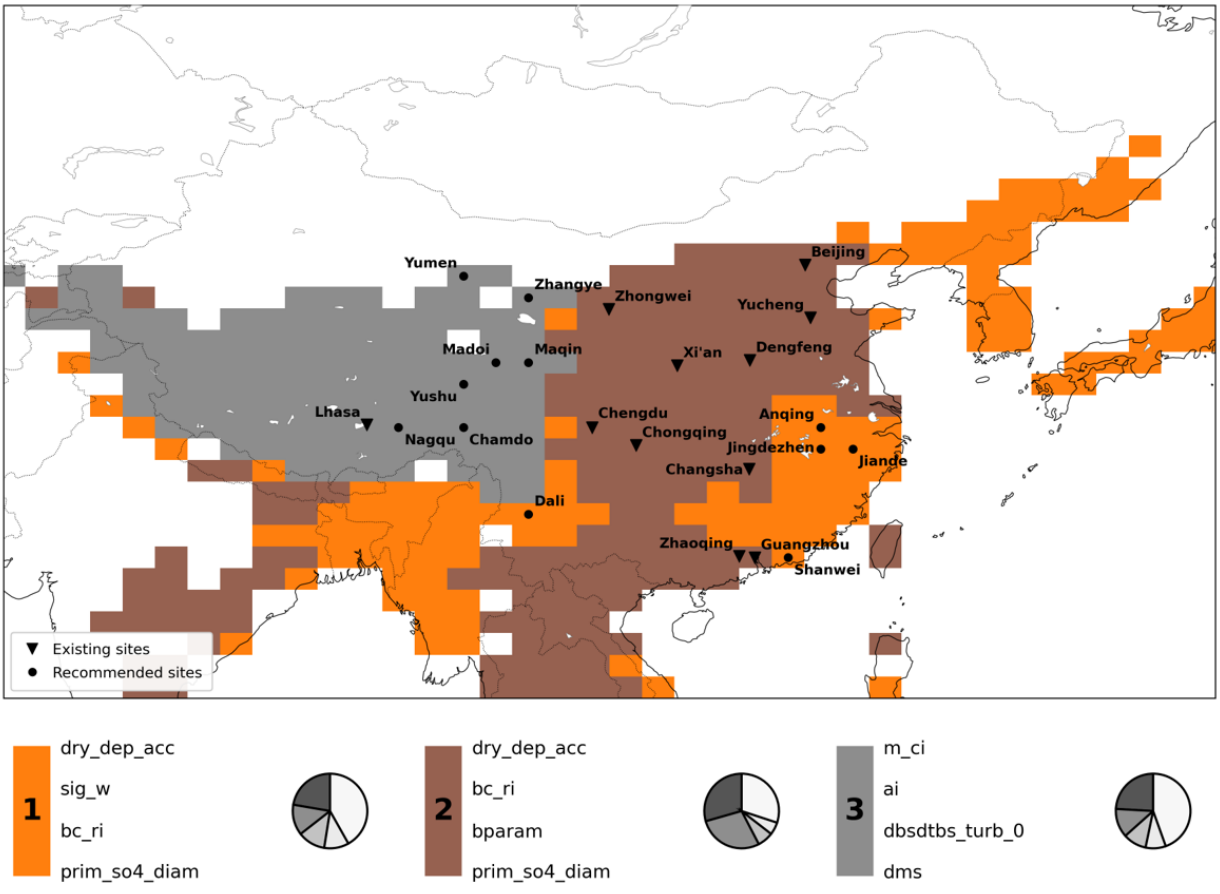


Figure 5: Candidate observation locations identified across the three land-based target clusters in China.

3.5 Synthetic constraint

In this section, we apply synthetic constraints on the remaining ΔF_{aci} uncertainty after the R23 optimal constraint within target clusters. Due to limited availability and the practical challenges introduced by using real observations (Regayre et al., 2023; Prévost et al., 2026a), we construct synthetic constraints for all of the seven observable variables described in Sect. 2.4, even where real observations are available at our target locations. This provides consistency in our constraint approach. We further evaluate the constraint potential of variables based on shared causes of remaining ΔF_{aci} uncertainty within each target cluster. This approach allows us to (a) select the order in which we apply synthetic constraints using observable variables and (b) provide guidance for future in-situ observations in target regions.

Here, we apply synthetic constraints to Clusters 1 and 2. Given the relatively small remaining uncertainty in Cluster 3 after the optimal constraint, combined with the sparsity of existing observation data, we do not synthetically constrain this cluster and instead rely on shared causes of uncertainty to provide guidance for future observations in this region.

https://doi.org/10.5194/egusphere-2026-7007
Preprint. Discussion started: 24 November 2026
© Author(s) 2026. CC BY 4.0 License.

In cluster 1, the key causes of remaining monthly and annual mean ΔF_{aci} uncertainty are the four parameters *dry_dep_acc*, *sig_w*, *bc_ri*, and *prim_so4_diam* (Fig. A5). Sensitivity analyses of observable variables reveal which aspects of ΔF_{aci} uncertainty may be constrained by individual observations (Fig. 6). N_d uncertainty is associated with the *sig_w* parameter. Constraining to match observed N_d in any of the target months at target cluster locations would constrain this aspect of ΔF_{aci} uncertainty. The *dry_dep_acc* parameter affects BC uncertainty most strongly (up to 70%), and other observable variables (OC, AOD, H_2SO_4 and AAOD) to a lesser extent. AAOD is clearly the target observable variable to constrain uncertainty associated with *bc_ri*. The *prim_so4_diam* parameter is only weakly represented by N_d in some target months and is not identified as important in any of the other variables. No single observational variable can be expected to fully constrain all the major causes of remaining ΔF_{aci} uncertainty, suggesting that the combination of multiple variables (with the exception of SO_2) can provide a more comprehensive and complementary set of uncertainty information, in line with previous constraint efforts (e.g. Regayre et al., 2020; Prévost et al., 2026b).

https://doi.org/10.5194/egusphere-2026-7007
Preprint. Discussion started: 24 November 2026
© Author(s) 2026. CC BY 4.0 License.

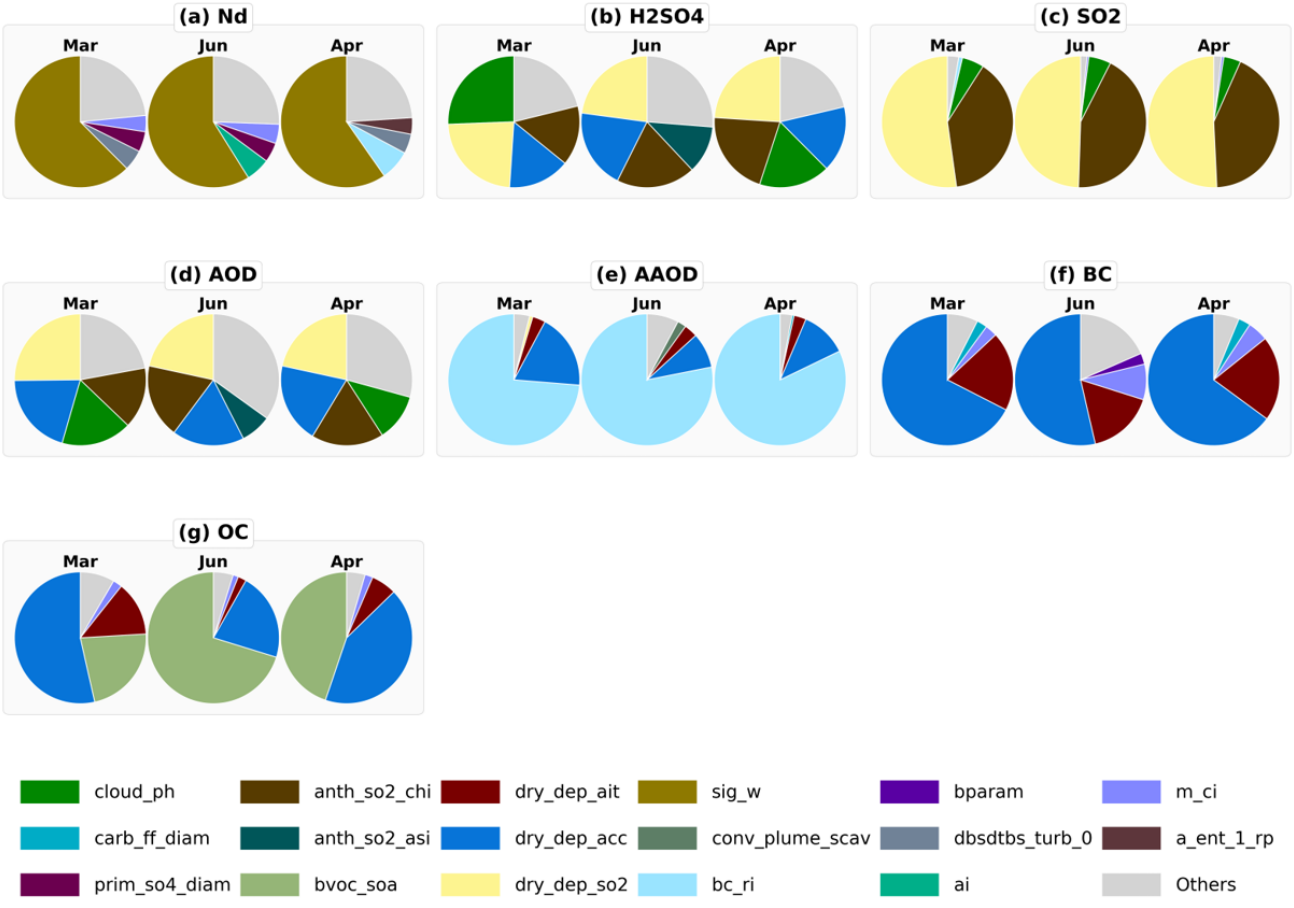


Figure 6: Monthly parameter uncertainty contributions to the variance of aerosol-relevant variables (a) N_d, (b) H_2SO_4, (c) SO_2, (d) AOD, (e) AAOD, (f) BC, and (g) OC over Cluster 1, based on GAM variance-based sensitivity analyses using the optimally constrained ensemble from R23. Each pie chart shows the relative contributions of the four most important uncertain parameters for the corresponding variable and month, calculated from the absolute signed responses. The remaining parameter contributions are grouped as "Others". Slices are arranged counterclockwise from the largest to the smallest contribution.

We progressively combine observable variable synthetic constraints following the approach described in Sect. 2.7 and informed by our evaluation of each variable's shared causes of uncertainty with ΔF_{aci} (Table 1). The largest cause of remaining annual mean ΔF_{aci} uncertainty in Cluster 1 is the *dry_dep_acc* parameter. Thus, BC is the first synthetic constraint we apply, reducing the number of model variants from five to four thousand in combination with the R23 optimal constraint. This targeted synthetic constraint further constrains ΔF_{aci} uncertainty by 5.0 %. We then systematically apply additional synthetic constraints in combination with BC and the R23 constraint. All additional variables are tested, and we retain the combined constraint that causes the strongest reduction in ΔF_{aci} uncertainty. In this case, the combination of synthetic N_d and AAOD observations provides the strongest constraint, reducing ΔF_{aci} uncertainty by a further 14.0 %, through the constraint on the updraft velocity (*sig_w*) parameter and the BC absorption (*bc_ri*) parameter. Additional synthetic constraints do not

https://doi.org/10.5194/egusphere-2026-7007
Preprint. Discussion started: 24 November 2026
© Author(s) 2026. CC BY 4.0 License.

510 meaningfully reduce ΔF_{aci} uncertainty, so we treat the BC, N_d, and AAOD combination as the maximum observational constraint in Cluster 1.

Table 1: Variable combination and reduction in remaining uncertainty for Cluster 1.

Variable combination	Reduction in remaining uncertainty (%)
BC	5.0
BC + N_d	12.7
BC + H_2SO_4	3.3
BC + SO_2	3.0
BC + AOD	3.5
BC + AAOD	7.2
BC + OC	4.7
BC + N_d + H_2SO_4	10.1
BC + N_d + SO_2	11.6
BC + N_d + AOD	10.1
BC + N_d + AAOD	**14.0**
BC + N_d + OC	12.1
BC + N_d + AAOD + H_2SO_4	11.8
BC + N_d + AAOD + SO_2	12.8
BC + N_d + AAOD + AOD	11.5
BC + N_d + AAOD + OC	13.1

515 Using this final variable combination, we further construct the tight synthetic constraint following the procedure described in Sect. 2.7. Finally, we could constrain the remaining ΔF_{aci} uncertainty in Cluster 1 by an additional 29% using these targeted observations compared with the R23 optimal constraint, constraining it to a range around -0.2 to 3 W m^{-2} (Table 2). Under idealised conditions, our tight synthetic constraint can reduce the original uncertainty in this region by around 64%.

https://doi.org/10.5194/egusphere-2026-7007
Preprint. Discussion started: 24 November 2026
© Author(s) 2026. CC BY 4.0 License.

Table 2: The 90% credible intervals of ΔF_{aci} for the Unconstrained, Optimal constraint, and Tight synthetic constraint, together with the corresponding reductions in uncertainty for Cluster 1.

	ΔF_{aci}	Reduction in remaining uncertainty after optimal constraint (%)	Reduction in original uncertainty (%)
Unconstrained	-2.3 to 6.7 W m^{-2}		
Optimal constraint	-1.5 to 3.1 W m^{-2}		
Tight synthetic constraint	-0.2 to 3.0 W m^{-2}	29.1%	63.8%

The remaining ΔF_{aci} uncertainty in Cluster 2 is mainly caused by the *dry_dep_acc*, *bc_ri*, *bparam*, and *prim_so4_diam* parameters (Fig. A6). Figure 7 shows that BC and OC are particularly sensitive to *dry_dep_acc*, and AOD, AAOD, and H_2SO_4 are also sensitive to this parameter. AAOD is the target variable for constraining ΔF_{aci} uncertainty associated with the *bc_ri* parameter, and N_d provides complementary information about ΔF_{aci} uncertainty associated with both *bc_ri* and *prim_so4_diam* parameters. In contrast, the observable variables identified for synthetic constraint are at best weakly sensitive to the *bparam* parameter (0.9 %), suggesting alternative observations will be needed to constrain this aspect of ΔF_{aci} uncertainty

https://doi.org/10.5194/egusphere-2026-7007
Preprint. Discussion started: 24 November 2026
© Author(s) 2026. CC BY 4.0 License.

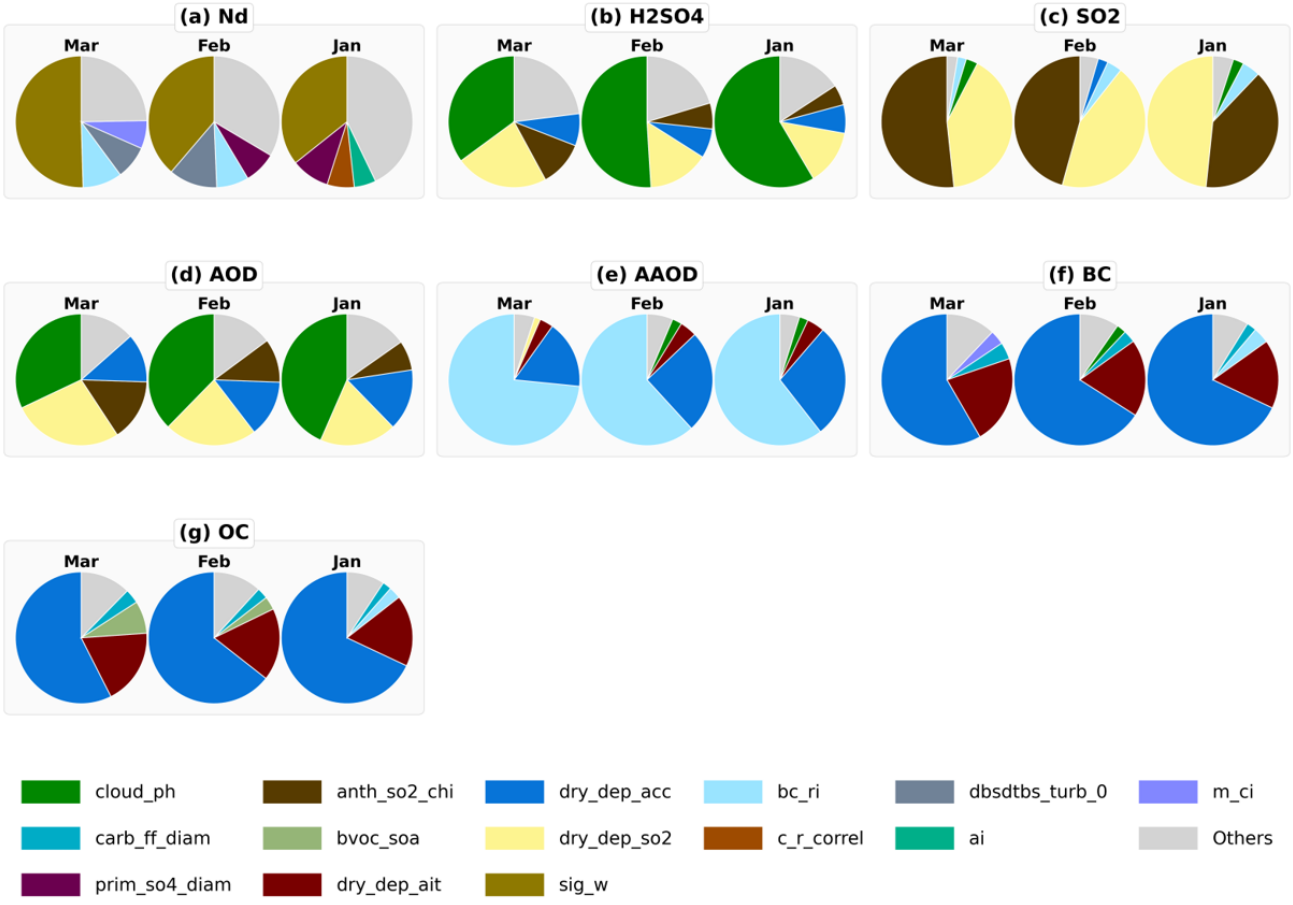


Figure 7: Monthly parameter uncertainty contributions to the variance of aerosol-relevant variables (a) N_d, (b) H_2SO_4, (c) SO_2, (d) AOD, (e) AAOD, (f) BC, and (g) OC over Cluster 2. All features are consistent with Fig. 6.

We therefore follow the same approach to assess how different combinations of observable variables reduce the remaining ΔF_{aci} uncertainty (Table 3). Both *dry_dep_acc* and *bc_ri* parameters are important contributors to the remaining ΔF_{aci} uncertainty in Cluster 2. We therefore first apply the synthetic constraint using AAOD, which provides good coverage of both parameters, reducing the number of model variants from 5000 to 4000 beyond the R23 optimal constraint. This targeted synthetic constraint further constrains ΔF_{aci} uncertainty by 16.5 %. We then systematically apply additional synthetic constraints in combination with AAOD and the R23 constraint. After testing all additional variables, we find that synthetic constraints using AAOD and N_d, as well as their combinations with BC or OC, achieve the greatest reduction in the remaining ΔF_{aci} uncertainty (approximately 20%). Other variable combinations do not meaningfully reduce the uncertainty. When applying tighter synthetic constraints, the combination of AAOD and N_d performs better than the combinations that also include BC or OC. The results suggest that AAOD already captures much of the uncertainty associated with

https://doi.org/10.5194/egusphere-2026-7007
Preprint. Discussion started: 24 November 2026
© Author(s) 2026. CC BY 4.0 License.

dry_dep_acc that BC and OC also represent. Adding these variables may therefore introduce redundant information and weaken the constraint. Thus, we treat the AAOD and N_d combination as the maximum observational constraint in Cluster 2.

Table 3: Variable combination and reduction in remaining uncertainty for Cluster 2.

Variable combination	Reduction in remaining uncertainty (%)
AAOD	16.5
AAOD + N_d	**19.6**
AAOD + H_2SO_4	9.1
AAOD + SO_2	10.5
AAOD + AOD	9.3
AAOD + BC	15.3
AAOD + OC	15.3
AAOD + N_d + H_2SO_4	14.6
AAOD + N_d + SO_2	16.9
AAOD + N_d + AOD	14.4
AAOD + N_d + BC	19.9
AAOD + N_d + OC	19.4

Based on the final variable combination, our tight synthetic constraint could reduce the remaining ΔF_{aci} uncertainty in Cluster 2 by an additional 49.2% compared with the R23 optimal constraint, constraining it to a range around 1.8 to 5.3 W m^{-2} (Table 4). The positive ΔF_{aci} in this region could be explained by the high black carbon concentrations, which can warm the atmosphere and affect clouds and boundary-layer stability, contributing to positive local radiative forcing (Shindell et al., 2013; Chen et al., 2025). Finally, our tight synthetic constraint can reduce the original uncertainty in this region by around 63%.

https://doi.org/10.5194/egusphere-2026-7007
Preprint. Discussion started: 24 November 2026
© Author(s) 2026. CC BY 4.0 License.

Table 4: The 90% credible intervals of ΔF_{aci} for the Unconstrained, Optimal constraint, and Tight synthetic constraint, together with the corresponding reductions in uncertainty for Cluster 2.

	ΔF_{aci}	Reduction in remaining uncertainty after optimal constraint (%)	Reduction in original uncertainty (%)
Unconstrained	-0.8 to 8.8 W m^{-2}		
Optimal constraint	-0.5 to 6.5 W m^{-2}		
Tight synthetic constraint	1.8 to 5.3 W m^{-2}	49.2%	62.6%

In Cluster 3, the key causes of remaining ΔF_{aci} uncertainty differ substantially from those in Clusters 1 and 2, with the largest contributions arising from the physical-atmosphere parameters *m_ci*, *ai*, and *dbsdtbs_turb_0*, together with the natural sulfur-emission parameter *dms* (Fig. A7). The observable variables evaluation (Fig. 8) shows that the observable variables we consider for synthetic constraint only modestly share causes of uncertainty with ΔF_{aci}. N_d is sensitive to the *m_ci* parameter, which causes between 9.2% and 14.2% of its variance across the three target months. N_d is also sensitive to *dbsdtbs_turb_0* in some months, as is SO_2. BC is sensitive to the *m_ci* parameter, which causes 5.5% of its variance in only one of the three target months. However, the uncertainty associated with *dms* is only weakly (0.7%) represented by the observable variables considered here. The main sensitivities of several other variables are mainly associated with parameters that are not among the key causes of the remaining ΔF_{aci} uncertainty in this cluster. Thus, although N_d and SO_2 provide limited potential for further ΔF_{aci} constraint, it is clear that additional observation types are needed. In particular, the relative importance of *m_ci*, *ai*, and *dbsdtbs_turb_0* parameters suggests that further ΔF_{aci} constraints could benefit from observations that more directly characterise cloud-ice microphysics and cloud dynamical processes.

https://doi.org/10.5194/egusphere-2026-7007
Preprint. Discussion started: 24 November 2026
© Author(s) 2026. CC BY 4.0 License.

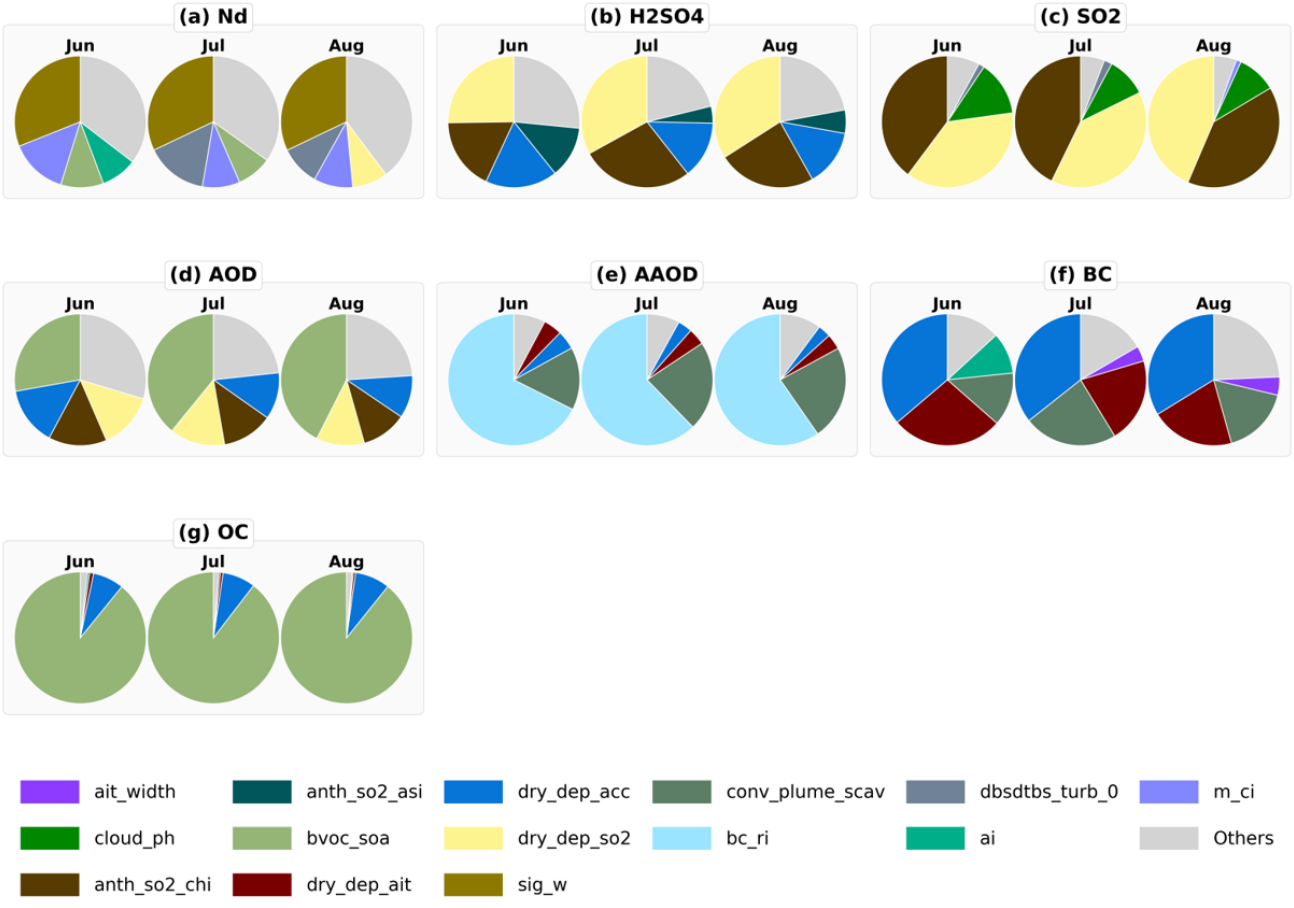


Figure 8: Monthly parameter uncertainty contributions to the variance of aerosol-relevant variables (a) N_d, (b) H_2SO_4, (c) SO_2, (d) AOD, (e) AAOD, (f) BC, and (g) OC over Cluster 3. All features are consistent with Fig. 6.

3.6 Evaluate the effects of the synthetic constraint

In this section, we evaluate the effects of the synthetic constraint in Clusters 1 and 2, including an exploration of changes in the magnitude, spatial distribution, and key causes of the remaining ΔF_{aci} uncertainty after applying our targeted synthetic constraints. After our synthetic constraint, we maximally constrain the annual-mean remaining ΔF_{aci} uncertainty by 29.0% in Cluster 1 and 49.2% in Cluster 2 relative to the optimal constraint, constraining it to a range around -0.2 to 3 W m^{-2} and 1.8 to 5.3 W m^{-2}, respectively. These tight constraints are achievable by retaining a very small subset of the original million model variants, which assumes precise, representative observations. These constraints demonstrate the benefits of identifying target observation locations and timings based on intensive model sensitivity analyses.

https://doi.org/10.5194/egusphere-2026-7007
Preprint. Discussion started: 24 November 2026
© Author(s) 2026. CC BY 4.0 License.

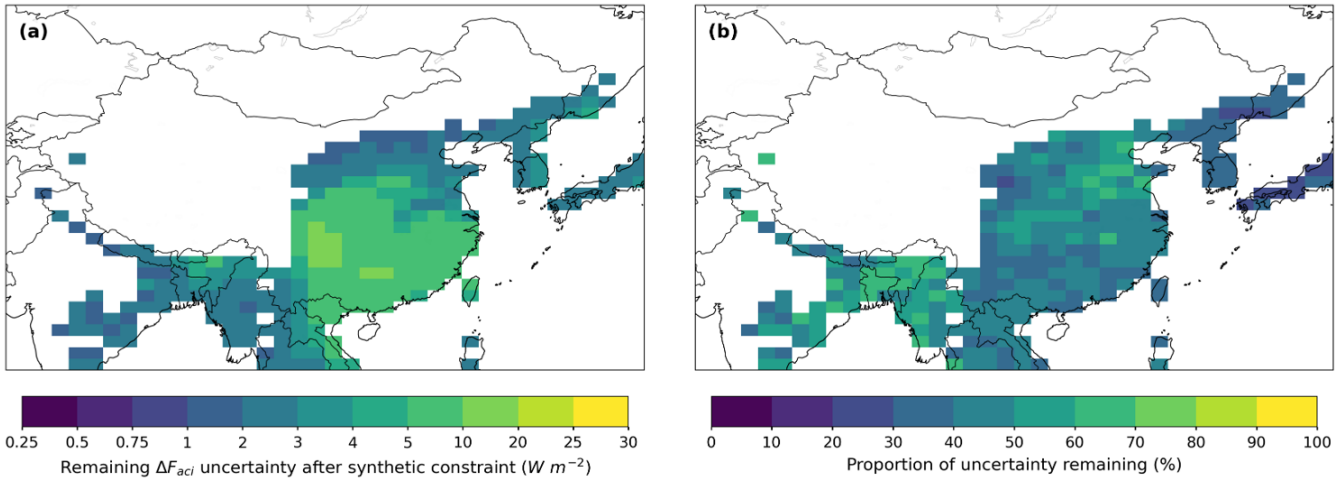


Figure 9: Annual mean ΔF_{aci} uncertainty (90 % credible interval ranges) in model grid boxes within Clusters 1 and 2 over China from (a) the final synthetic constrained set of model variants, as well as (b) the proportion of original uncertainty remaining after the synthetic constraints.

Figure 9 shows the spatial distribution of the remaining ΔF_{aci} uncertainty after applying the synthetic constraints. Compared with the R23 optimal constraint, the original uncertainty decreases by at least 40 % in all regions and by up to 80 % locally. Overall, our tight synthetic constraint could constrain the original uncertainty by around 60% within these regions. The effects of the synthetic constraint are particularly clear over the high remaining uncertainty region within the Sichuan Basin, where the remaining uncertainty reduces by around 70 % to around 10 to 20 W m^{-2}. The distinct high-value band extending eastward from the Sichuan Basin across central China, which indicates strong remaining uncertainty in these regions, is no longer evident after applying the synthetic constraint. Meanwhile, the remaining uncertainty across central, eastern, and coastal China is generally reduced to around 5 to 10 W m^{-2}, with only a few areas close to Hunan and Guangxi provinces remaining at around 10 W m^{-2}. In parts of northern and northeastern China, the synthetic constraint further reduces the remaining uncertainty to 3 W m^{-2} or less.

https://doi.org/10.5194/egusphere-2026-7007
Preprint. Discussion started: 24 November 2026
© Author(s) 2026. CC BY 4.0 License.

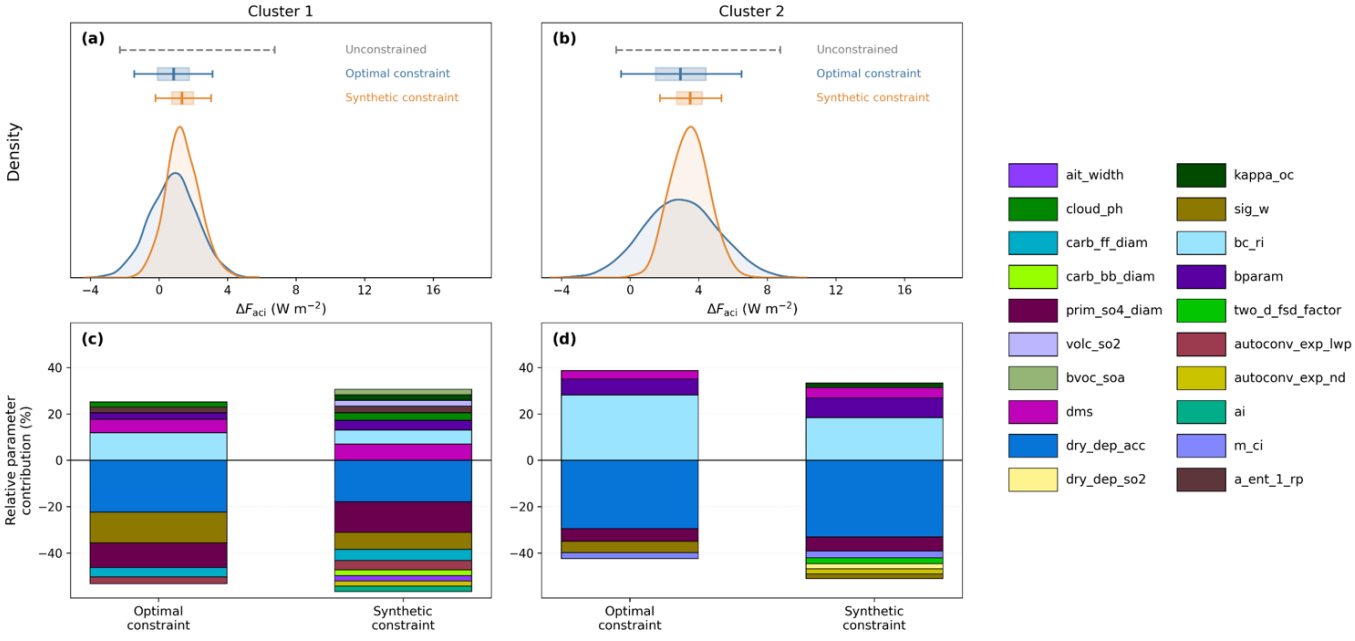


Figure 10: Annual-mean ΔF_{aci} distributions and dominant parametric contributions to the remaining uncertainty across Clusters 1 and 2. (a, b) Probability density functions under the optimal and additional synthetic constraints. Horizontal box plots show the 5th, 25th, 50th, 75th, and 95th percentiles, while grey dashed lines indicate the unconstrained 5th–95th percentile ranges. (c, d) Relative parameter contributions under the optimal and synthetic constraints. Positive and negative contributions are stacked separately, with only parameters contributing more than 2% shown.

Figure 10 shows how the key causes of the annual-mean remaining ΔF_{aci} uncertainty change after the synthetic constraint. In Cluster 1, the contributions of *bc_ri* and *sig_w* particularly decrease after the synthetic constraint, while the *dry_dep_acc* parameter decreases but remains important. The contributions of the *prim_so4_diam* parameter slightly increase after the synthetic constraint, suggesting that primary sulfate particle size and its influence on cloud droplet formation become relatively more important. Changes in the relative importance of parameters after observational constraints are applied are a known phenomenon used to target additional constraint variables (Regayre et al., 2026). Several previously unimportant parameters become more prominent, including *volc_so2*, *carb_bb_diam*, *kappa_oc*, and *bvoc_soa*. However, the 90% credible intervals for cluster mean uncertainty are reduced from 4.6 to 3.2 W m^{-2}, and the remaining uncertainty is shared between multiple parameters, suggesting the synthetic constraints are approaching the maximum feasible constraint. Further constraints in Cluster 1 should combine observations associated with *dry_dep_acc*, *prim_so4_diam*, aerosol properties, and natural background aerosol sources.

In Cluster 2, the key causes of uncertainty remain *dry_dep_acc*, *bc_ri*, *bparam*, and *prim_so4_diam* after the synthetic constraint, as was the case after the R23 constraint. The 90% credible intervals for cluster mean uncertainty are reduced from 7.0 to 3.5 W m^{-2}. However, the relative importance of these parameters as causes of uncertainty changes substantially. The

https://doi.org/10.5194/egusphere-2026-7007
Preprint. Discussion started: 24 November 2026
© Author(s) 2026. CC BY 4.0 License.

bc_ri parameter decreases in importance from 28.2% to 18.4%, whereas *dry_dep_acc* accounts for a larger variance, increasing from 29.4% to 33.1%. The relative contribution from *bparam* also increases, while *prim_so4_diam* remains important. These changes suggest that the combination of synthetic observed variables we selected targets important components of the remaining uncertainty structure. But some processes related to aerosol removal and cloud processing need additional observations to achieve maximum constraint. Further constraints in Cluster 2 should therefore place greater emphasis on observations associated with persistent causes of uncertainty related to aerosol removal and radiative properties.

4 Conclusion

The R23 optimal constraint reduced global annual-mean ΔF_{aci} uncertainty by nearly 70%, but its effect was spatially heterogeneous and did little to reduce the substantial uncertainty over Asia (Regayre et al., 2023, 2026). The remaining ΔF_{aci} uncertainty after the optimal constraint is between 50 % and 100 % over most of China, with the weakest constraint over the densely populated regions of central and eastern China. So, even after being 'optimally' constrained, future projections based on these model variants are susceptible to substantial regional uncertainties with potentially global effects (Smith et al., 2016). Here, we develop a framework to identify when, where, and which additional observations can further constrain the remaining ΔF_{aci} uncertainty over China. We identify target novel and existing observations that share causes of model uncertainty with ΔF_{aci} and use synthetic observations to quantify the potential impact of such observations on ΔF_{aci} uncertainty.

Our synthetic constraints further reduce the annual-mean remaining ΔF_{aci} uncertainty by around 30 % in Cluster 1 (eastern coastal China) and around 50 % in Cluster 2 (central China) relative to the R23 optimal constraint, constraining it to a range around -0.2 to 3 W m^{-2} and 1.8 to 5.3 W m^{-2} respectively, substantially constraining the persistent uncertainty across China (Fig. 9). We do not quantify synthetic constraint in Cluster 3 (western China) because the original and remaining uncertainty are both relatively small and the causes of model uncertainty are unrelated to the observable variables considered for constraint here. We identify target months and locations in all clusters to inform future observation campaign priorities.

Applying synthetic constraints changes the relative importance of the parameters contributing to the remaining ΔF_{aci} uncertainty. In Cluster 1, *dry_dep_acc* remains the most important cause of remaining uncertainty, while the relative contribution of the updraft parameter *sig_w* decreases from 13.3% to 7.3% and the black carbon refractive index parameter *bc_ri* decreases from 11.9% to 6.1%. Whereas those of *prim_so4_diam* and *dms* increase slightly. These results indicate an increased importance of natural sulfur emissions and background aerosol concentrations, as anthropogenic sources and droplet activation are constrained, in agreement with Carslaw et al. (2013). In Cluster 2, *dry_dep_acc*, *bc_ri*, *bparam*, and *prim_so4_diam* remain the four most important parameters, but the contribution of *bc_ri* decreases, whereas *dry_dep_acc* and *bparam* become more prominent. This reordering of key causes of remaining uncertainty suggests that further constraint

https://doi.org/10.5194/egusphere-2026-7007
Preprint. Discussion started: 24 November 2026
© Author(s) 2026. CC BY 4.0 License.

should prioritise aerosol deposition and cloud physical processes. These results suggest that achieving maximum constraint on ΔF_{aci} will require systematic implementation of (a) evaluation of causes of uncertainty, (b) identification of priority observation types and locations, and (c) application of targeted constraints.

Our results suggest that multiple collocated observations at target locations and months are more valuable than many individual observations of the same type distributed across a region. We identify target locations for constraint using sensitivity analyses over our large set of model variants, grouping model outputs into regions of shared causes of uncertainty, and quantifying the representativeness of each location. Complementary measurements made at the same target locations, such as near-surface BC, N_{d}, and AAOD, jointly constrain different aspects of the processes that cause ΔF_{aci} uncertainty in our synthetic constraints. Such observations are costly: near-surface BC measurements require sustained instrument operation and maintenance, N_{d} often requires expensive aircraft campaigns, and AAOD can be retrieved using lidar but remains highly uncertain. However, we believe this approach is necessary if we are to tackle the persistent uncertainty in ΔF_{aci} and improve model skill at making climate projections. Future observational efforts should therefore support both collocated measurements of key variables at target locations and improvements in measurement quality.

We use synthetic constraints here to quantify the maximum constraint achievable within one climate model. Our results represent the potential information content of novel observations rather than the constraint that would necessarily be achieved using real measurements. Real-world application of our approach will introduce multiple complicating factors, including observational uncertainty, spatial and temporal representation errors, and model structural deficiencies, which can cause otherwise informative observations to provide inconsistent constraints (Schutgens et al., 2017; Regayre et al., 2023; Prévost et al., 2026a). In addition, our analysis is mainly based on the 37 parameters of UKESM1, so our results here may not transfer directly to other climate models or newer versions of this model. Hence, future work should test this framework using real collocated observations and evaluate its robustness across other models and broader causes of uncertainty.

https://doi.org/10.5194/egusphere-2026-7007
Preprint. Discussion started: 24 November 2026
© Author(s) 2026. CC BY 4.0 License.

Appendix A

Table A1: Parameter names, perturbation type, and description, following Regayre et al. (2023).

Parameter name	Perturbation type	Description
bl_nuc	Aerosol process	Boundary layer nucleation rate scale factor
ait_width	Aerosol process	Modal width of Aitken modes
cloud_drop_acidity	Aerosol process	Cloud droplet acidity
carb_ff_diam	Aerosol process	Emission diameter of carbonaceous aerosol from fossil fuel sources
carb_bb_diam	Natural aerosol emission	Emission diameter of carbonaceous aerosol from biomass burning sources
carb_res_diam	Anthropogenic aerosol emission	Emission diameter of carbonaceous aerosol from residential sources
prim_so4_diam	Anthropogenic aerosol emission	Emission diameter of 50 % of new sub-grid sulfate particles. Remaining 50 % emitted into the larger coarse mode
sea_salt	Natural aerosol emission	Sea salt emission flux scale factor
anth_so2_chi	Anthropogenic aerosol emission	Anthropogenic SO_2 emission flux scale factor - China
anth_so2_asi	Anthropogenic aerosol emission	Anthropogenic SO_2 emission flux scale factor - Asia
anth_so2_eur	Anthropogenic aerosol emission	Anthropogenic SO_2 emission flux scale factor - Europe
anth_so2_nam	Anthropogenic aerosol emission	Anthropogenic SO_2 emission flux scale factor - North America
anth_so2_r	Anthropogenic aerosol emission	Anthropogenic SO_2 emission flux scale factor - Rest of the world
volc_so2	Natural aerosol emission	Volcanic SO_2 emission flux scale factor
bvoc_soa	Natural aerosol emission	Biogenic monoterpene production rate of secondary organic aerosol scale factor
dms	Natural aerosol emission	Dimethyl-sulfide emission flux scale factor
prim_moc	Natural aerosol emission	Primary marine organic carbon emission flux scale factor
dry_dep_ait	Aerosol process	Dry deposition velocity of Aitken mode aerosol
dry_dep_acc	Aerosol process	Dry deposition velocity of accumulation mode aerosol
dry_dep_so2	Aerosol process	Dry deposition velocity of SO_2
kappa_oc	Aerosol process	Hygroscopicity parameter (κ) for organic aerosol
sig_w	Aerosol process	Standard deviation of shallow-cloud updraft velocity scale factor
rain_frac	Aerosol process	Fraction of cloud covered area where rain removes aerosol
cloud_ice_thresh	Aerosol process	Threshold of cloud ice water fraction for scavenging
conv_plume_scav	Aerosol process	Scavenging efficiency (as a fraction of total aerosol removed) of Aitken mode aerosol in convective clouds
bc_ri	Aerosol process	Imaginary part of the black carbon refractive index
oxidants_oh	Aerosol process	Offline oxidant OH concentration scale factor

https://doi.org/10.5194/egusphere-2026-7007
Preprint. Discussion started: 24 November 2026
© Author(s) 2026. CC BY 4.0 License.

oxidants_o3	Aerosol process	Offline oxidant O_3 concentration scale factor
bparam	Physical atmosphere	Coefficient of the spectral shape parameter (β) for effective radius
two_d_fsd_factor	Physical atmosphere	Scale factor for the 2D relationship between cloud condensate variance, cloud cover and convection - Controls sub-grid cloud heterogeneity
c_r_correl	Physical atmosphere	Cloud and rain sub-grid horizontal spatial colocation
autoconv_exp_lwp	Physical atmosphere	Exponent of liquid water path in the power law for initiating autoconversion
autoconv_exp_nd	Physical atmosphere	Exponent of cloud droplet concentration (N_d) in the power law for initiating autoconversion
dbsdtbs_turb_0	Physical atmosphere	Cloud erosion rate
ai	Physical atmosphere	Scaling coefficient for the dependence of ice mass on diameter
m_ci	Physical atmosphere	Ice fall speed scale factor
a_ent_1_rp	Physical atmosphere	Cloud top entrainment rate scale factor

680

https://doi.org/10.5194/egusphere-2026-7007
Preprint. Discussion started: 24 November 2026
© Author(s) 2026. CC BY 4.0 License.

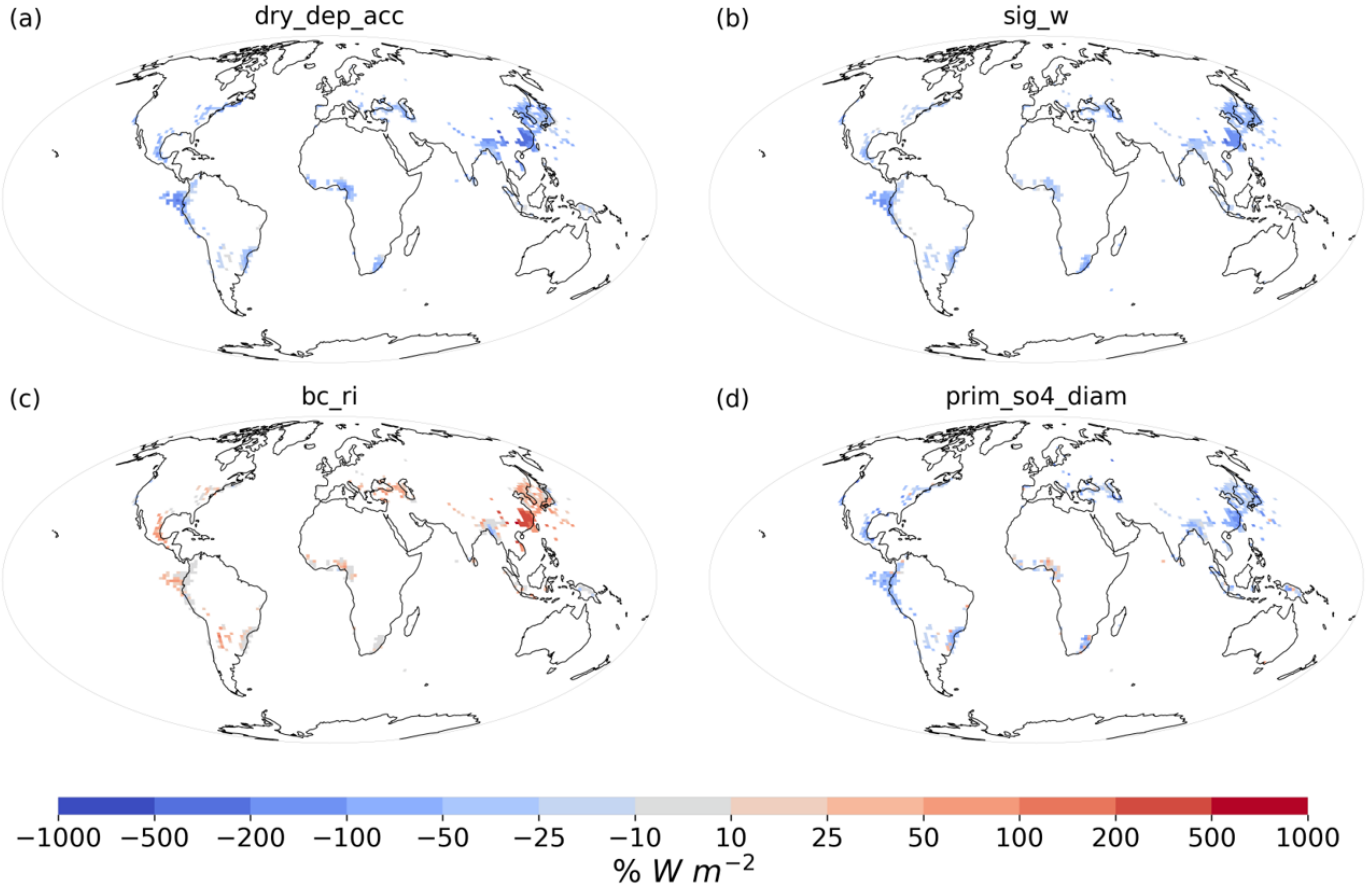
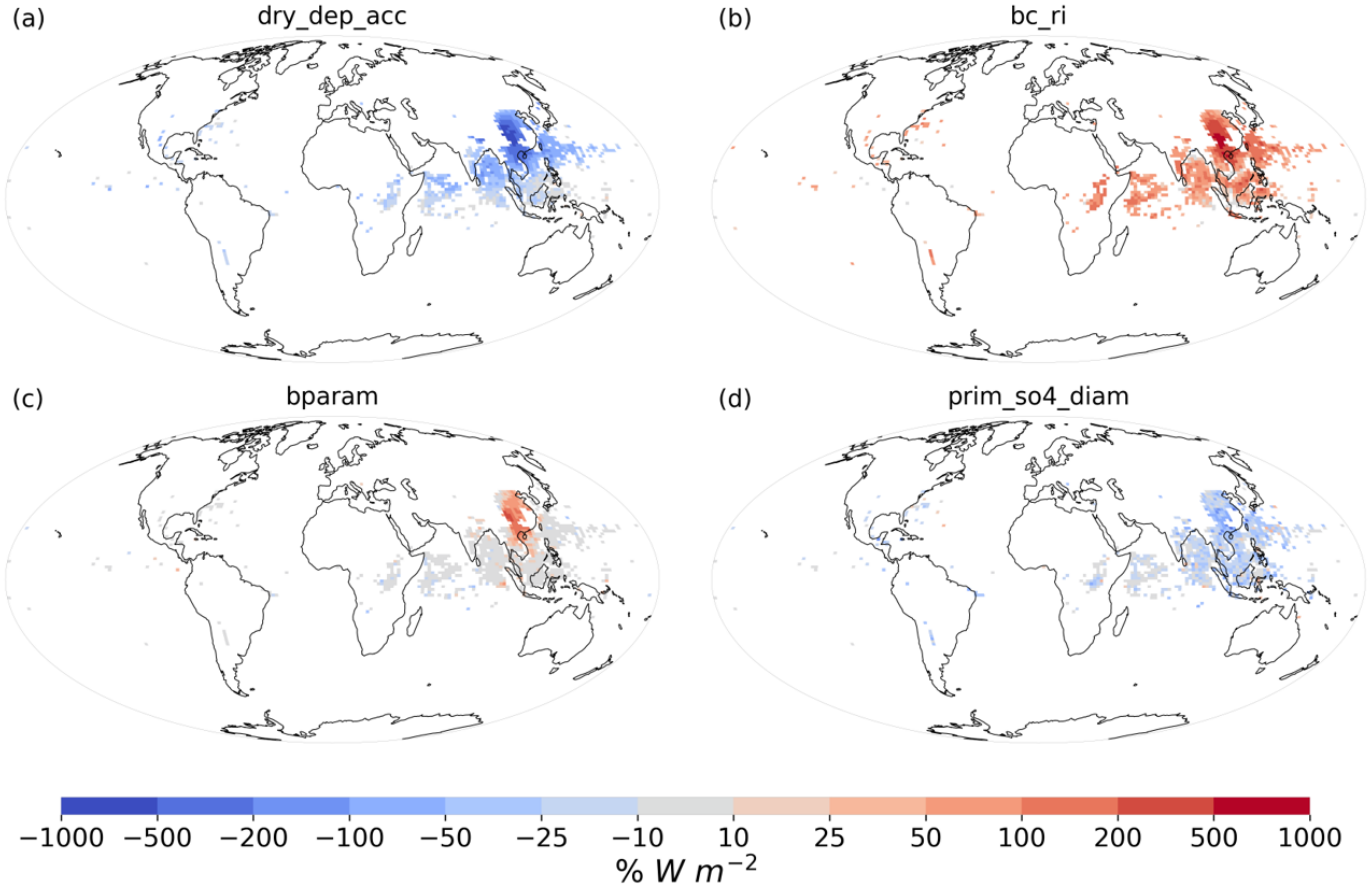


Figure A1: Maps of key parametric causes of the remaining ΔF_{aci} uncertainty after the R23 optimal constraint in global cluster 1. Shading indicates the proportion of ΔF_{aci} uncertainty caused by individual parameters, multiplied by the 90 % credible interval (CI) range in that grid box and by the sign of the ΔF_{aci} response to increasing the parameter value. Negative values indicate that increasing the parameter value is associated with stronger (more negative) ΔF_{aci}. Regions where the ΔF_{aci} 90 % CI is less than 3 W m^{-2} are masked.

https://doi.org/10.5194/egusphere-2026-7007
Preprint. Discussion started: 24 November 2026
© Author(s) 2026. CC BY 4.0 License.



690 **Figure A2: Maps of key parametric causes of the remaining ΔF_{aci} uncertainty after the R23 optimal constraint in global cluster 2. All features are consistent with Fig. A1.**

https://doi.org/10.5194/egusphere-2026-7007
Preprint. Discussion started: 24 November 2026
© Author(s) 2026. CC BY 4.0 License.

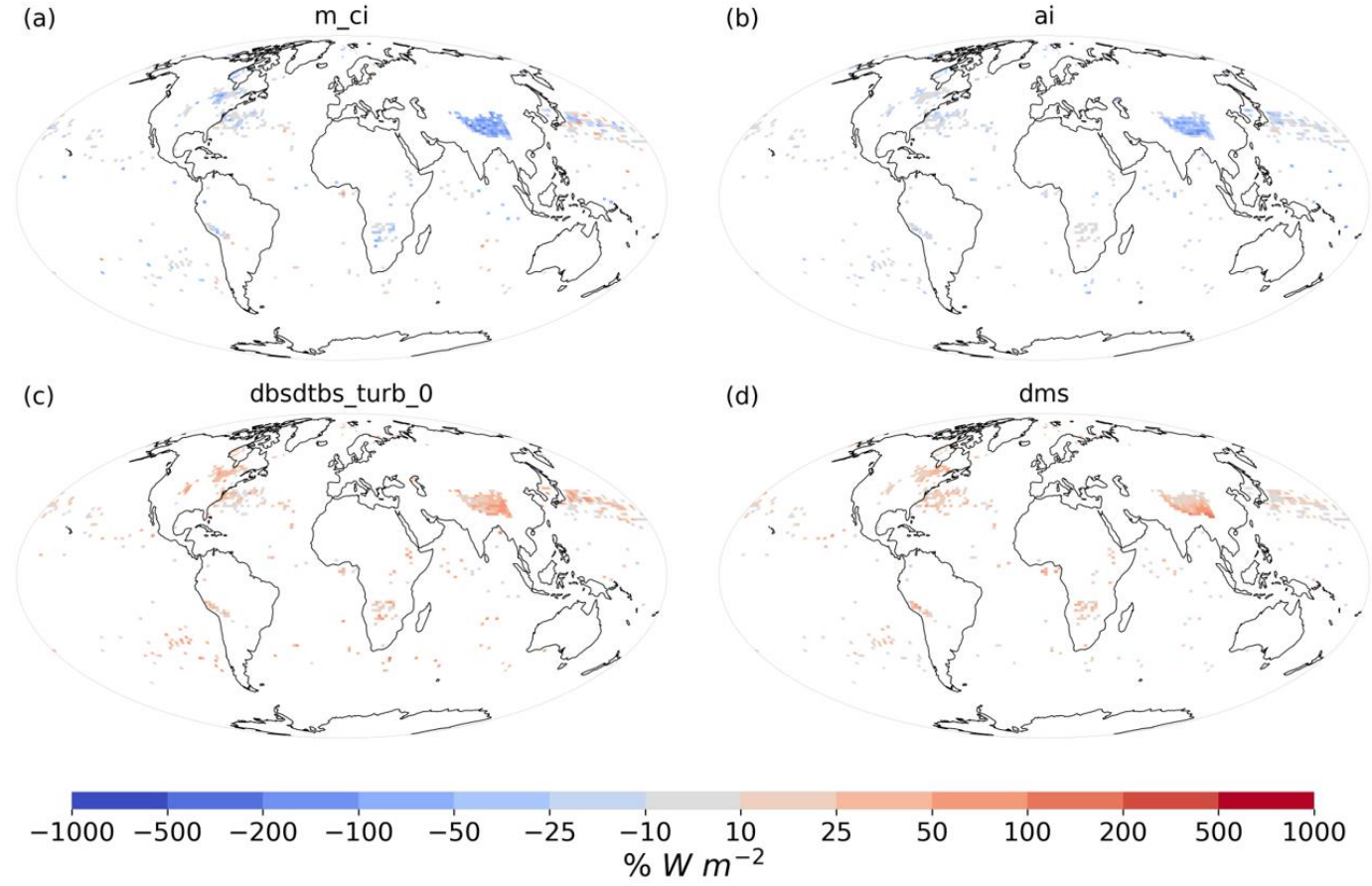


Figure A3: Maps of key parametric causes of the remaining ΔF_{aci} uncertainty after the R23 optimal constraint in global cluster 3. All features are consistent with Fig. A1.

https://doi.org/10.5194/egusphere-2026-7007
Preprint. Discussion started: 24 November 2026
© Author(s) 2026. CC BY 4.0 License.

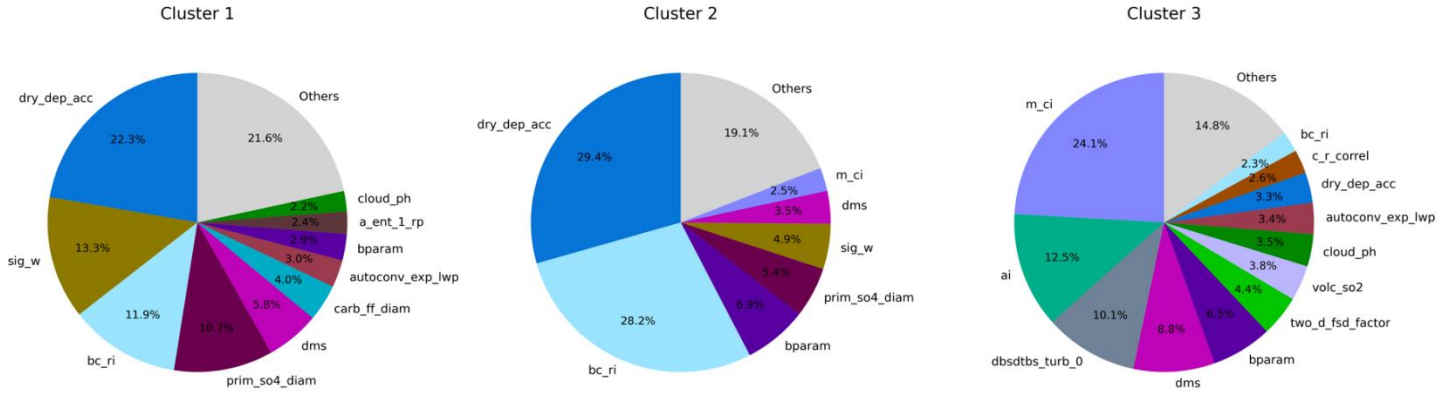


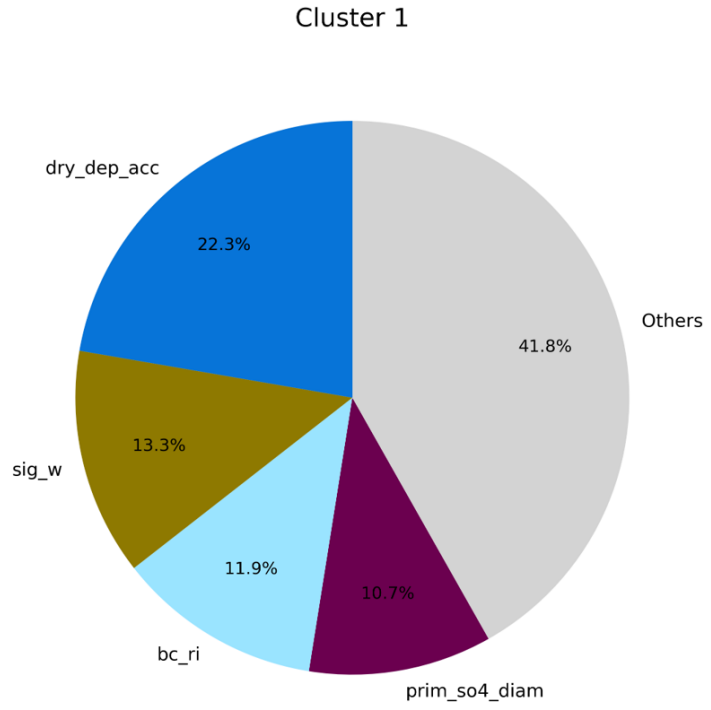
Figure A4: Relative contributions of the key causes of uncertainty to ΔF_{aci} across the three land-based clusters over China. For each cluster, only parameters contributing more than 2% to the cluster-level ΔF_{aci} variance are shown. Each sector represents the relative contribution of one parameter, with larger sectors indicating a stronger influence on the remaining aerosol-cloud forcing uncertainty. These cluster-specific parameter-contribution structures also provide the basis for the subsequent similarity analysis.

https://doi.org/10.5194/egusphere-2026-7007
Preprint. Discussion started: 24 November 2026
© Author(s) 2026. CC BY 4.0 License.

Table A2: The Site name, Cluster attribution, Site type, Latitude, and Longitude of candidate observation locations.

Site name	Cluster	Site type	Latitude (°N)	Longitude (°E)
Anqing	1	Recommended	30.62	117.19
Dali	1	Recommended	25.62	100.31
Jingdezhen	1	Recommended	29.38	117.19
Jiande	1	Recommended	29.38	119.06
Shanwei	1	Recommended	23.12	115.31
Beijing	2	Existing	39.38	117.19
Changsha	2	Existing	28.12	113.44
Chengdu	2	Existing	30.62	104.06
Chongqing	2	Existing	29.38	105.94
Dengfeng	2	Existing	34.38	113.44
Guangzhou	2	Existing	23.12	113.44
Xi'an	2	Existing	34.38	109.69
Yucheng	2	Existing	36.88	117.19
Zhaoqing	2	Existing	23.12	111.56
Zhongwei	2	Existing	36.88	104.06
Chamdo	3	Recommended	30.62	96.56
Lhasa	3	Existing	30.62	90.94
Madoi	3	Recommended	34.38	98.44
Maqin	3	Recommended	34.38	100.31
Nagqu	3	Recommended	30.62	92.81
Yumen	3	Recommended	39.38	96.56
Yushu	3	Recommended	33.12	96.56
Zhangye	3	Recommended	38.12	100.31

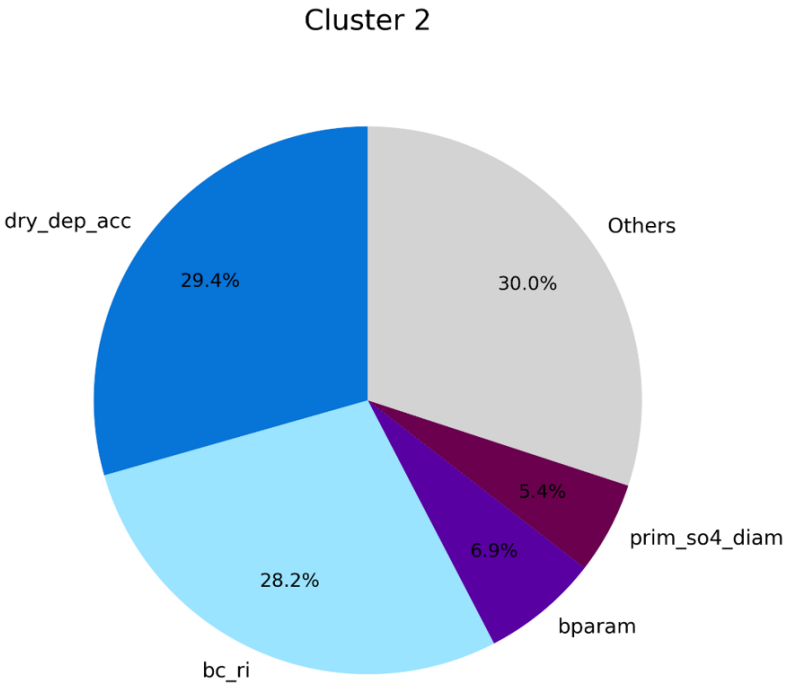
https://doi.org/10.5194/egusphere-2026-7007
Preprint. Discussion started: 24 November 2026
© Author(s) 2026. CC BY 4.0 License.



705

Figure A5: Relative contributions of the key causes of uncertainty to ΔF_{aci} in Cluster 1. Only the top 4 parameters are shown. Each sector represents the relative contribution of one parameter, with larger sectors indicating a stronger influence on the remaining aerosol-cloud forcing uncertainty.

https://doi.org/10.5194/egusphere-2026-7007
Preprint. Discussion started: 24 November 2026
© Author(s) 2026. CC BY 4.0 License.



710

Figure A6: Relative contributions of the key causes of uncertainty to ΔF_{aci} in Cluster 2. All features are consistent with Fig. A5.

https://doi.org/10.5194/egusphere-2026-7007
Preprint. Discussion started: 24 November 2026
© Author(s) 2026. CC BY 4.0 License.

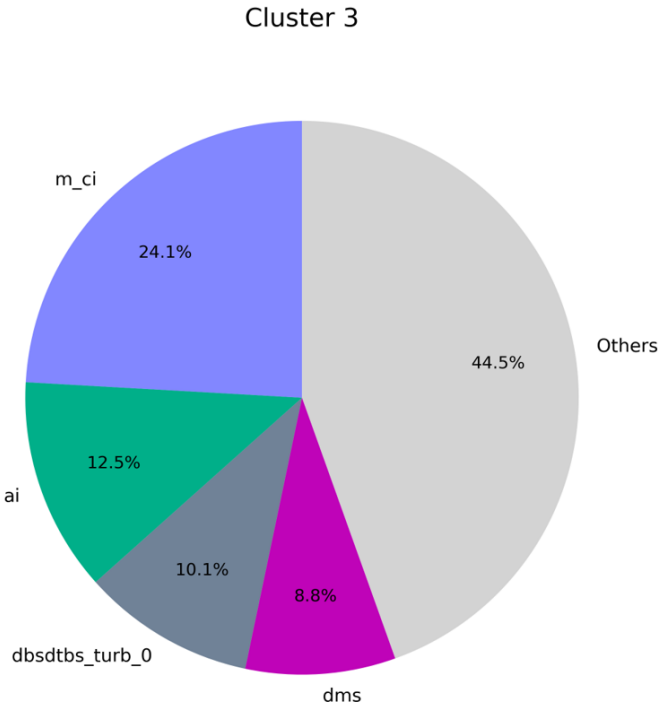


Figure A7: Relative contributions of the key causes of uncertainty to ΔF_{aci} in Cluster 3. All features are consistent with Fig. A5.

Code availability

Code used to create figures in this article is available here: https://github.com/Jianxing-Luo/The-code-for-Identifying-observations-to-maximize-aerosol-radiative-forcing-constraint-over-China.git

Data availability

Output from the A-CURE PPE is available on the CEDA archive (https://catalogue.ceda.ac.uk/uuid/b735718d66c1403fbf6b93ba3bd3b1a9, Regayre et al.,2021).

Author contributions

JL and LR developed the original ideas and conceptualised the study. Code for emulation was based on input from LR. Code for GAM analyses and Statistical emulators was adapted by JL from source code provided by LR. K-means clusters were adapted by JL with source code and input from LP and LR. JL created the statistical emulators and GAM variances at the grid box level, re-evaluated regional K-means clusters, evaluated observations by time and location, and applied synthetic

https://doi.org/10.5194/egusphere-2026-7007
Preprint. Discussion started: 24 November 2026
© Author(s) 2026. CC BY 4.0 License.

constraints. LR provided overarching guidance and helped interpret results. LP and KG contributed through discussions. The original draft was written by JL and LR, and reviewed by all co-authors.

Competing interests

The authors declare that they have no conflicts of interest.

Acknowledgements

The PPE that informed this research was created using the ARCHER UK National Supercomputing Service (http://www.archer.ac.uk, last accessed 21 January 2021) under project allocation n02-NEP013406. This work used JASMIN, the UK's collaborative data analysis environment (https://www.jasmin.ac.uk). This work originated as part of JL's MRes project at the University of Leeds, under the supervision of LR.

Financial support

Leighton A. Regayre was supported by the Met Office Hadley Centre Climate Programme funded by DSIT. Léa M. C. Prévost was supported by the NERC Panorama Doctoral Training Partnership with additional CASE sponsorship from the Met Office (grant no. NE/S007458/1, project reference 2886996). We acknowledge funding from NERC under grants A-CURE and Aerosol-MFR (NE/P013406/1 and NE/X013901/1).

References

Andres, R. J. and Kasgnoc, A. D.: A time-averaged inventory of subaerial volcanic sulfur emissions, J. Geophys. Res., 103, 25251–25261, https://doi.org/10.1029/98JD02091, 1998.

Andreae, M. O., Jones, C. D., and Cox, P. M.: Strong present-day aerosol cooling implies a hot future, Nature, 435, 1187–1190, https://doi.org/10.1038/nature03671, 2005.

Archibald, A. T., O'Connor, F. M., Abraham, N. L., Archer-Nicholls, S., Chipperfield, M. P., Dalvi, M., Folberth, G. A., Dennison, F., Dhomse, S. S., Griffiths, P. T., Hardacre, C., Hewitt, A. J., Hill, R. S., Johnson, C. E., Keeble, J., Köhler, M. O., Morgenstern, O., Mulcahy, J. P., Ordóñez, C., Pope, R. J., Rumbold, S. T., Russo, M. R., Savage, N. H., Sellar, A., Stringer, M., Turnock, S. T., Wild, O., and Zeng, G.: Description and evaluation of the UKCA stratosphere–troposphere chemistry scheme (StratTrop vn 1.0) implemented in UKESM1, Geoscientific Model Development, 13, 1223–1266, https://doi.org/10.5194/gmd-13-1223-2020, 2020.

https://doi.org/10.5194/egusphere-2026-7007
Preprint. Discussion started: 24 November 2026
© Author(s) 2026. CC BY 4.0 License.

Beven, K. and Freer, J.: Equifinality, data assimilation, and uncertainty estimation in mechanistic modelling of complex environmental systems using the GLUE methodology, Journal of Hydrology, 249, 11–29, https://doi.org/10.1016/S0022-1694(01)00421-8, 2001.

Balkanski, Y., Schulz, M., Claquin, T., and Guibert, S.: Reevaluation of Mineral aerosol radiative forcings suggests a better agreement with satellite and AERONET data, Atmospheric Chemistry and Physics, 7, 81–95, https://doi.org/10.5194/acp-7-81-2007, 2007.

Browse, J., Carslaw, K. S., Arnold, S. R., Pringle, K., and Boucher, O.: The scavenging processes controlling the seasonal cycle in Arctic sulphate and black carbon aerosol, Atmospheric Chemistry and Physics, 12, 6775–6798, https://doi.org/10.5194/acp-12-6775-2012, 2012.

Bond, T. C., Doherty, S. J., Fahey, D. W., Forster, P. M., Berntsen, T., DeAngelo, B. J., Flanner, M. G., Ghan, S., Kärcher, B., Koch, D., Kinne, S., Kondo, Y., Quinn, P. K., Sarofim, M. C., Schultz, M. G., Schulz, M., Venkataraman, C., Zhang, H., Zhang, S., Bellouin, N., Guttikunda, S. K., Hopke, P. K., Jacobson, M. Z., Kaiser, J. W., Klimont, Z., Lohmann, U., Schwarz, J. P., Shindell, D., Storelvmo, T., Warren, S. G., and Zender, C. S.: Bounding the role of black carbon in the climate system: A scientific assessment, Journal of Geophysical Research: Atmospheres, 118, 5380–5552, https://doi.org/10.1002/jgrd.50171, 2013.

Bellouin, N., Quaas, J., Morcrette, J.-J., and Boucher, O.: Estimates of aerosol radiative forcing from the MACC re-analysis, Atmospheric Chemistry and Physics, 13, 2045–2062, https://doi.org/10.5194/acp-13-2045-2013, 2013.

Berger, S., Caud, N., Chen, Y., Goldfarb, L., Gomis, M. I., Huang, M., Leitzell, K., Lon noy, E., Matthews, J. B. R., Maycock, T. K., Aterfield, T., Yelekci, O., Yu, R., and Zhou, B., Cambridge University Press, https://doi.org/10.1017/9781009157896.009, 2021.

Bhatti, Y. A., Watson-Parris, D., Regayre, L. A., Jia, H., Neubauer, D., Im, U., Svenhag, C., Schutgens, N., Tsikerdekis, A., Nenes, A., Irfan, M., van Diedenhoven, B., Arifi, A., Fu, G., and Hasekamp, O. P.: Uncertainty in aerosol effective radiative forcing from anthropogenic and natural aerosol parameters in ECHAM6.3-HAM2.3, Atmospheric Chemistry and Physics, 26, 269–293, https://doi.org/10.5194/acp-26-269-2026, 2026.

Carslaw, K. S., Lee, L. A., Reddington, C. L., Pringle, K. J., Rap, A., Forster, P. M., Mann, G. W., Spracklen, D. V., Woodhouse, M. T., Regayre, L. A., and Pierce, J. R.: Large contribution of natural aerosols to uncertainty in indirect forcing, Nature, 503, 67–71, https://doi.org/10.1038/nature12674, 2013.

Carslaw, K., Lee, L., Regayre, L., and Johnson, J.: Climate Models Are Uncertain, but We Can Do Something About It, Eos, 99, https://doi.org/10.1029/2018EO093757, 2018.

Chen, Y., Turnock, S. T., Scott, C. E., and Arnold, S. R.: Radiative Response to Large Decline in Anthropogenic Emissions From China Between 2008 and 2016 Is Modified by Simultaneous Biomass Burning Emission Changes, Journal of Geophysical Research: Atmospheres, 130, e2025JD044548, https://doi.org/10.1029/2025JD044548, 2025.

Carslaw, K. S., Regayre, L. A., Proske, U., Gettelman, A., Sexton, D. M. H., Qian, Y., Marshall, L. R., Wild, O., van Lier-Walqui, M., Oertel, A., Peatier, S., Yang, B., Johnson, J. S., Li, S., McCoy, D. T., Sanderson, B. M., Williamson, C. J.,

https://doi.org/10.5194/egusphere-2026-7007
Preprint. Discussion started: 24 November 2026
© Author(s) 2026. CC BY 4.0 License.

Elsaesser, G. S., Yamazaki, K., and Booth, B. B. B.: Opinion: The importance and future development of perturbed parameter ensembles in climate and atmospheric science, Atmospheric Chemistry and Physics, 26, 4651–4667, https://doi.org/10.5194/acp-26-4651-2026, 2026.

Eyring, V., Bony, S., Meehl, G. A., Senior, C. A., Stevens, B., Stouffer, R. J., and Taylor, K. E.: Overview of the Coupled Model Intercomparison Project Phase 6 (CMIP6) experimental design and organization, Geoscientific Model Development, 9, 1937–1958, https://doi.org/10.5194/gmd-9-1937-2016, 2016.

Eidhammer, T., Gettelman, A., Thayer-Calder, K., Watson-Parris, D., Elsaesser, G., Morrison, H., van Lier-Walqui, M., Song, C., and McCoy, D.: An extensible perturbed parameter ensemble for the Community Atmosphere Model version 6, Geoscientific Model Development, 17, 7835–7853, https://doi.org/10.5194/gmd-17-7835-2024, 2024.

Forster, P., Storelvmo, T., Armour, K., Collins, W., Dufresne, J., Frame, D., Lunt, D., Mauritsen, T., Palmer, M., Watanabe, M., Wild, M., and Zhang, H.: The Earth's energy budget, climate feedbacks, and climate sensitivity, in: Climate Change 2021: The Physical Science Basis. Contribution of Working Group I to the Sixth Assessment Report of the Intergovernmental Panel on Climate Change, edited by: Masson-Delmotte, V., Zhai, P., Pi rani, A., Connors, S. L., Pean, C.,

Fyfe, J. C., Kharin, V. V., Santer, B. D., Cole, J. N. S., and Gillett, N. P.: Significant impact of forcing uncertainty in a large ensemble of climate model simulations, Proceedings of the National Academy of Sciences, 118, e2016549118, https://doi.org/10.1073/pnas.2016549118, 2021.

Gosling, J. P.: SHELF: The Sheffield Elicitation Framework, in: Elicitation: The Science and Art of Structuring Judgement, edited by: Dias, L. C., Morton, A., and Quigley, J., Springer International Publishing, Cham, 61–93, https://doi.org/10.1007/978-3-319-65052-4_4, 2018.

Grosvenor, D. P. and Carslaw, K. S.: The decomposition of cloud–aerosol forcing in the UK Earth System Model (UKESM1), Atmospheric Chemistry and Physics, 20, 15681–15724, https://doi.org/10.5194/acp-20-15681-2020, 2020.

Ghan, S., Wang, M., Zhang, S., Ferrachat, S., Gettelman, A., Griesfeller, J., Kipling, Z., Lohmann, U., Morrison, H., Neubauer, D., Partridge, D. G., Stier, P., Takemura, T., Wang, H., and Zhang, K.: Challenges in constraining anthropogenic aerosol effects on cloud radiative forcing using present-day spatiotemporal variability, Proceedings of the National Academy of Sciences, 113, 5804–5811, https://doi.org/10.1073/pnas.1514036113, 2016.

Gao, J., Yang, Y., Wang, H., Wang, P., Li, B., Li, J., Wei, J., Gao, M., and Liao, H.: Climate responses in China to domestic and foreign aerosol changes due to clean air actions during 2013–2019, npj Clim Atmos Sci, 6, 160, https://doi.org/10.1038/s41612-023-00488-y, 2023.

Gettelman, A., Eidhammer, T., Duffy, M. L., McCoy, D. T., Song, C., and Watson-Parris, D.: The Interaction Between Climate Forcing and Feedbacks, Journal of Geophysical Research: Atmospheres, 129, e2024JD040857, https://doi.org/10.1029/2024JD040857, 2024.

Halmer, M. M., Schmincke, H.-U., and Graf, H.-F.: The annual volcanic gas input into the atmosphere, in particular into the stratosphere: a global data set for the past 100 years, Journal of Volcanology and Geothermal Research, 115, 511–528, https://doi.org/10.1016/S0377-0273(01)00318-3, 2002.

https://doi.org/10.5194/egusphere-2026-7007
Preprint. Discussion started: 24 November 2026
© Author(s) 2026. CC BY 4.0 License.

Johnson, J. S., Regayre, L. A., Yoshioka, M., Pringle, K. J., Turnock, S. T., Browse, J., Sexton, D. M. H., Rostron, J. W., Schutgens, N. A. J., Partridge, D. G., Liu, D., Allan, J. D., Coe, H., Ding, A., Cohen, D. D., Atanacio, A., Vakkari, V., Asmi, E., and Carslaw, K. S.: Robust observational constraint of uncertain aerosol processes and emissions in a climate model and the effect on aerosol radiative forcing, Atmospheric Chemistry and Physics, 20, 9491–9524, https://doi.org/10.5194/acp-20-9491-2020, 2020.

Lin, L. I.-K.: A Concordance Correlation Coefficient to Evaluate Reproducibility, Biometrics, 45, 255, https://doi.org/10.2307/2532051, 1989.

Lee, L. A., Reddington, C. L., and Carslaw, K. S.: On the relationship between aerosol model uncertainty and radiative forcing uncertainty, Proceedings of the National Academy of Sciences, 113, 5820–5827, https://doi.org/10.1073/pnas.1507050113, 2016.

Li, Z. Q., Xu, H., Li, K. T., Li, D. H., Xie, Y. S., Li, L., Zhang, Y., Gu, X. F., Zhao, W., Tian, Q. J., Deng, R. R., Su, X. L., Huang, B., Qiao, Y. L., Cui, W. Y., Hu, Y., Gong, C. L., Wang, Y. Q., Wang, X. F., Wang, J. P., Du, W. B., Pan, Z. Q., Li, Z. Z., and Bu, D.: Comprehensive Study of Optical, Physical, Chemical, and Radiative Properties of Total Columnar Atmospheric Aerosols over China: An Overview of Sun–Sky Radiometer Observation Network (SONET) Measurements, Bulletin of the American Meteorological Society, 99, 739–755, https://doi.org/10.1175/BAMS-D-17-0133.1, 2018.

Metzger, A., Verheggen, B., Dommen, J., Duplissy, J., Prevot, A. S. H., Weingartner, E., Riipinen, I., Kulmala, M., Spracklen, D. V., Carslaw, K. S., and Baltensperger, U.: Evidence for the role of organics in aerosol particle formation under atmospheric conditions, Proceedings of the National Academy of Sciences, 107, 6646–6651, https://doi.org/10.1073/pnas.0911330107, 2010.

Moosavi, V., Aschwanden, G., and Velasco, E.: Finding candidate locations for aerosol pollution monitoring at street level using a data-driven methodology, Atmospheric Measurement Techniques, 8, 3563–3575, https://doi.org/10.5194/amt-8-3563-2015, 2015.

Mulcahy, J. P., Jones, C., Sellar, A., Johnson, B., Boutle, I. A., Jones, A., Andrews, T., Rumbold, S. T., Mollard, J., Bellouin, N., Johnson, C. E., Williams, K. D., Grosvenor, D. P., and McCoy, D. T.: Improved Aerosol Processes and Effective Radiative Forcing in HadGEM3 and UKESM1, Journal of Advances in Modeling Earth Systems, 10, 2786–2805, https://doi.org/10.1029/2018MS001464, 2018.

Mulcahy, J. P., Johnson, C., Jones, C. G., Povey, A. C., Scott, C. E., Sellar, A., Turnock, S. T., Woodhouse, M. T., Abraham, N. L., Andrews, M. B., Bellouin, N., Browse, J., Carslaw, K. S., Dalvi, M., Folberth, G. A., Glover, M., Grosvenor, D. P., Hardacre, C., Hill, R., Johnson, B., Jones, A., Kipling, Z., Mann, G., Mollard, J., O'Connor, F. M., Palmiéri, J., Reddington, C., Rumbold, S. T., Richardson, M., Schutgens, N. A. J., Stier, P., Stringer, M., Tang, Y., Walton, J., Woodward, S., and Yool, A.: Description and evaluation of aerosol in UKESM1 and HadGEM3-GC3.1 CMIP6 historical simulations, Geoscientific Model Development, 13, 6383–6423, https://doi.org/10.5194/gmd-13-6383-2020, 2020.

https://doi.org/10.5194/egusphere-2026-7007
Preprint. Discussion started: 24 November 2026
© Author(s) 2026. CC BY 4.0 License.

McCoy, D., Wood, R., Burrows, S. M., Fridlind, A., Igel, A., Jen, C., Regayre, L., Saito, M., and Watson-Parris, D.: Micro2Macro: Origins of Climate Change Uncertainty: A US CLIVAR Workshop Report, U.S. CLIVAR Project Office, Report 2025-6, 64 pp., https://doi.org/10.5065/q8f4-yc54, 2025.

O'Hagan, A.: Bayesian analysis of computer code outputs: A tutorial, Reliability Engineering & System Safety, 91, 1290–1300, https://doi.org/10.1016/j.ress.2005.11.025, 2006.

Pearson, K.: VII. Mathematical contributions to the theory of evolution.—III. Regression, heredity, and panmixia, Phil. Trans. R. Soc. A, 253–318, https://doi.org/10.1098/rsta.1896.0007, 1896.

Peace, A. H., Carslaw, K. S., Lee, L. A., Regayre, L. A., Booth, B. B. B., Johnson, J. S., and Bernie, D.: Effect of aerosol radiative forcing uncertainty on projected exceedance year of a 1.5 °C global temperature rise, Environ. Res. Lett., 15, 0940a6, https://doi.org/10.1088/1748-9326/aba20c, 2020.

Prévost, L. M. C., Regayre, L. A., Johnson, J. S., McNeall, D., Milton, S., and Carslaw, K. S.: Detection of potential structural deficiencies in a global aerosol model using a perturbed parameter ensemble, Atmospheric Chemistry and Physics, 26, 2487–2530, https://doi.org/10.5194/acp-26-2487-2026, 2026a.

Prévost, L. M. C., Regayre, L., Ghosh, K., Johnson, J. S., Webb, I., Owen, J., Oakley, J., McNeall, D. J., Milton, S. F., and Carslaw, K. S.: Structural Model Deficiencies Impose a Fundamental Limit on Uncertainty Reduction of Aerosol Forcing, https://doi.org/10.22541/essoar.15009265/v1, 22 September 2026., 2026b.

Regayre, L. A., Pringle, K. J., Booth, B. B. B., Lee, L. A., Mann, G. W., Browse, J., Woodhouse, M. T., Rap, A., Reddington, C. L., and Carslaw, K. S.: Uncertainty in the magnitude of aerosol-cloud radiative forcing over recent decades, Geophysical Research Letters, 41, 9040–9049, https://doi.org/10.1002/2014GL062029, 2014.

Regayre, L. A., Pringle, K. J., Lee, L. A., Rap, A., Browse, J., Mann, G. W., Reddington, C. L., Carslaw, K. S., Booth, B. B. B., and Woodhouse, M. T.: The Climatic Importance of Uncertainties in Regional Aerosol–Cloud Radiative Forcings over Recent Decades, Journal of Climate, 28, 6589–6607, https://doi.org/10.1175/JCLI-D-15-0127.1, 2015.

Regayre, L. A., Johnson, J. S., Yoshioka, M., Pringle, K. J., Sexton, D. M. H., Booth, B. B. B., Lee, L. A., Bellouin, N., and Carslaw, K. S.: Aerosol and physical atmosphere model parameters are both important sources of uncertainty in aerosol ERF, Atmospheric Chemistry and Physics, 18, 9975–10006, https://doi.org/10.5194/acp-18-9975-2018, 2018.

Regayre, L. A., Carslaw, K. S., Deaconu, L., Symonds, C., Richardson, M., Langton, T., Watson-Parris, D., and Stier, P.: A-CURE: Monthly mean perturbed parameter ensemble data, https://catalogue.ceda.ac.uk/uuid/b735718d66c1403fbf6b93ba3bd3b1a9 (last access: 10 February 2026), 2021.

Regayre, L. A., Deaconu, L., Grosvenor, D. P., Sexton, D. M. H., Symonds, C., Langton, T., Watson-Paris, D., Mulcahy, J. P., Pringle, K. J., Richardson, M., Johnson, J. S., Rostron, J. W., Gordon, H., Lister, G., Stier, P., and Carslaw, K. S.: Identifying climate model structural inconsistencies allows for tight constraint of aerosol radiative forcing, Atmospheric Chemistry and Physics, 23, 8749–8768, https://doi.org/10.5194/acp-23-8749-2023, 2023.

https://doi.org/10.5194/egusphere-2026-7007
Preprint. Discussion started: 24 November 2026
© Author(s) 2026. CC BY 4.0 License.

Regayre, L. A., Prévost, L. M. C., Ghosh, K., Johnson, J. S., Oakley, J. E., Owen, J., Webb, I., and Carslaw, K. S.: Remaining aerosol forcing uncertainty after observational constraint and the processes that cause it, Atmospheric Chemistry and Physics, 26, 2293–2317, https://doi.org/10.5194/acp-26-2293-2026, 2026.

Schutgens, N. A. J.: Site representativity of AERONET and GAW remotely sensed aerosol optical thickness and absorbing aerosol optical thickness observations, Atmospheric Chemistry and Physics, 20, 7473–7488, https://doi.org/10.5194/acp-20-7473-2020, 2020.

Servén, D. and Brummitt, C.: pyGAM: Generalized Additive Models in Python, https://doi.org/10.5281/zenodo.1208724, 2018.

Shindell, D. T., Lamarque, J.-F., Schulz, M., Flanner, M., Jiao, C., Chin, M., Young, P. J., Lee, Y. H., Rotstayn, L., Mahowald, N., Milly, G., Faluvegi, G., Balkanski, Y., Collins, W. J., Conley, A. J., Dalsoren, S., Easter, R., Ghan, S., Horowitz, L., Liu, X., Myhre, G., Nagashima, T., Naik, V., Rumbold, S. T., Skeie, R., Sudo, K., Szopa, S., Takemura, T., Voulgarakis, A., Yoon, J.-H., and Lo, F.: Radiative forcing in the ACCMIP historical and future climate simulations, Atmospheric Chemistry and Physics, 13, 2939–2974, https://doi.org/10.5194/acp-13-2939-2013, 2013.

Seinfeld, J. H., Bretherton, C., Carslaw, K. S., Coe, H., DeMott, P. J., Dunlea, E. J., Feingold, G., Ghan, S., Guenther, A. B., Kahn, R., Kraucunas, I., Kreidenweis, S. M., Molina, M. J., Nenes, A., Penner, J. E., Prather, K. A., Ramanathan, V., Ramaswamy, V., Rasch, P. J., Ravishankara, A. R., Rosenfeld, D., Stephens, G., and Wood, R.: Improving our fundamental understanding of the role of aerosol−cloud interactions in the climate system, Proceedings of the National Academy of Sciences, 113, 5781–5790, https://doi.org/10.1073/pnas.1514043113, 2016.

Smith, D. M., Booth, B. B. B., Dunstone, N. J., Eade, R., Hermanson, L., Jones, G. S., Scaife, A. A., Sheen, K. L., and Thompson, V.: Role of volcanic and anthropogenic aerosols in the recent global surface warming slowdown, Nature Clim Change, 6, 936–940, https://doi.org/10.1038/nclimate3058, 2016.

Schutgens, N., Tsyro, S., Gryspeerdt, E., Goto, D., Weigum, N., Schulz, M., and Stier, P.: On the spatio-temporal representativeness of observations, Atmospheric Chemistry and Physics, 17, 9761–9780, https://doi.org/10.5194/acp-17-9761-2017, 2017.

Sellar, A. A., Jones, C. G., Mulcahy, J. P., Tang, Y., Yool, A., Wiltshire, A., O'Connor, F. M., Stringer, M., Hill, R., Palmieri, J., Woodward, S., de Mora, L., Kuhlbrodt, T., Rumbold, S. T., Kelley, D. I., Ellis, R., Johnson, C. E., Walton, J., Abraham, N. L., Andrews, M. B., Andrews, T., Archibald, A. T., Berthou, S., Burke, E., Blockley, E., Carslaw, K., Dalvi, M., Edwards, J., Folberth, G. A., Gedney, N., Griffiths, P. T., Harper, A. B., Hendry, M. A., Hewitt, A. J., Johnson, B., Jones, A., Jones, C. D., Keeble, J., Liddicoat, S., Morgenstern, O., Parker, R. J., Predoi, V., Robertson, E., Siahaan, A., Smith, R. S., Swaminathan, R., Woodhouse, M. T., Zeng, G., and Zerroukat, M.: UKESM1: Description and Evaluation of the U.K. Earth System Model, Journal of Advances in Modeling Earth Systems, 11, 4513–4558, https://doi.org/10.1029/2019MS001739, 2019.

https://doi.org/10.5194/egusphere-2026-7007
Preprint. Discussion started: 24 November 2026
© Author(s) 2026. CC BY 4.0 License.

Sexton, D. M. H., McSweeney, C. F., Rostron, J. W., Yamazaki, K., Booth, B. B. B., Murphy, J. M., Regayre, L., Johnson, J. S., and Karmalkar, A. V.: A perturbed parameter ensemble of HadGEM3-GC3.05 coupled model projections: part 1: selecting the parameter combinations, Clim. Dyn., 56, 3395–3436, https://doi.org/10.1007/s00382-021-05709-9, 2021.

Watson-Parris, D. and Smith, C. J.: Large uncertainty in future warming due to aerosol forcing, Nat. Clim. Chang., 12, 1111–1113, https://doi.org/10.1038/s41558-022-01516-0, 2022.

Williams, K. D., Copsey, D., Blockley, E. W., Bodas-Salcedo, A., Calvert, D., Comer, R., Davis, P., Graham, T., Hewitt, H. T., Hill, R., Hyder, P., Ineson, S., Johns, T. C., Keen, A. B., Lee, R. W., Megann, A., Milton, S. F., Rae, J. G. L., Roberts, M. J., Scaife, A. A., Schiemann, R., Storkey, D., Thorpe, L., Watterson, I. G., Walters, D. N., West, A., Wood, R. A., Woollings, T., and Xavier, P. K.: The Met Office Global Coupled Model 3.0 and 3.1 (GC3.0 and GC3.1) Configurations, Journal of Advances in Modeling Earth Systems, 10, 357–380, https://doi.org/10.1002/2017MS001115, 2018.

Walters, D., Baran, A. J., Boutle, I., Brooks, M., Earnshaw, P., Edwards, J., Furtado, K., Hill, P., Lock, A., Manners, J., Morcrette, C., Mulcahy, J., Sanchez, C., Smith, C., Stratton, R., Tennant, W., Tomassini, L., Van Weverberg, K., Vosper, S., Willett, M., Browse, J., Bushell, A., Carslaw, K., Dalvi, M., Essery, R., Gedney, N., Hardiman, S., Johnson, B., Johnson, C., Jones, A., Jones, C., Mann, G., Milton, S., Rumbold, H., Sellar, A., Ujiie, M., Whitall, M., Williams, K., and Zerroukat, M.: The Met Office Unified Model Global Atmosphere 7.0/7.1 and JULES Global Land 7.0 configurations, Geoscientific Model Development, 12, 1909–1963, https://doi.org/10.5194/gmd-12-1909-2019, 2019.

Watson-Parris, D., Bellouin, N., Deaconu, L. T., Schutgens, N. a. J., Yoshioka, M., Regayre, L. A., Pringle, K. J., Johnson, J. S., Smith, C. J., Carslaw, K. S., and Stier, P.: Constraining Uncertainty in Aerosol Direct Forcing, Geophysical Research Letters, 47, e2020GL087141, https://doi.org/10.1029/2020GL087141, 2020.

Xin, J., Wang, Y., Pan, Y., Ji, D., Liu, Z., Wen, T., Wang, Y., Li, X., Sun, Y., Sun, J., Wang, P., Wang, G., Wang, X., Cong, Z., Song, T., Hu, B., Wang, L., Tang, G., Gao, W., Guo, Y., Miao, H., Tian, S., and Wang, L.: The Campaign on Atmospheric Aerosol Research Network of China: CARE-China, Bulletin of the American Meteorological Society, 96, 1137–1155, https://doi.org/10.1175/BAMS-D-14-00039.1, 2015.

Yoshioka, M., Regayre, L. A., Pringle, K. J., Johnson, J. S., Mann, G. W., Partridge, D. G., Sexton, D. M. H., Lister, G. M. S., Schutgens, N., Stier, P., Kipling, Z., Bellouin, N., Browse, J., Booth, B. B. B., Johnson, C. E., Johnson, B., Mollard, J. D. P., Lee, L., and Carslaw, K. S.: Ensembles of Global Climate Model Variants Designed for the Quantification and Constraint of Uncertainty in Aerosols and Their Radiative Forcing, Journal of Advances in Modeling Earth Systems, 11, 3728–3754, https://doi.org/10.1029/2019MS001628, 2019.

Zhuang, B. L., Liu, L., Shen, F. H., Wang, T. J., and Han, Y.: Semidirect radiative forcing of internal mixed black carbon cloud droplet and its regional climatic effect over China, Journal of Geophysical Research: Atmospheres, 115, https://doi.org/10.1029/2009JD013165, 2010.